

FORCED CONVECTION WITH MICRO-POROUS CHANNELS
AND NANOFUID: EXPERIMENTAL AND NUMERICAL
STUDY

by

Cayley Sachi Delisle

Bachelor of Engineering in Mechanical Engineering, Ryerson University, 2017

A thesis

presented to Ryerson University

in partial fulfillment of the

requirements for the degree of

Master of Applied Science

in the program of

Mechanical and Industrial Engineering

Toronto, Ontario, Canada, 2019

©Cayley Sachi Delisle, 2019

AUTHOR'S DECLARATION FOR ELECTRONIC SUBMISSION OF A THESIS

I hereby declare that I am the sole author of this thesis. This is a true copy of the thesis, including any required final revisions, as accepted by my examiners.

I authorized Ryerson University to lend this thesis to other institutions or individuals for the purpose of scholarly research.

I further authorize Ryerson University to reproduce this thesis by photocopying or by other means, in total or in part, at the request of the other institutions or individuals for the purpose of scholarly research.

I understand that my thesis may be made electronically available to the public.

Abstract

Forced Convection with Micro-Porous Channels and Nanofluid: Experimental and Numerical Study

Master of Applied Science 2019

Cayley Sachi Delisle

Mechanical and Industrial Engineering

Ryerson University

This paper will investigate the heat transfer enhancement potential of micro-porous channels and nanofluid concentrations. The test blocks are two and three channels, that have 10 and 20 PPI foam metal inserts. The working fluids used are nanofluid with 0.6% alumina and distilled water. There are three flow rates used for the experiment, 0.1, 0.2 and 0.3 USGPM. The maximum average Nusselt number is 135.5, thus having the best rate removal of thermal energy. The pressure drop is an important result because it indicates how much pumping power is required. A lower pressure drop requires less power, which reduces operating costs. The lowest pressure drop is 0.97. Another observation, the temperature distribution has optimal results for the cases with nanofluid with 0.6% alumina and three-channels at a flow rate of 0.3 USGPM. Finally, the experimental and numerical studies are in good agreement with an average relative error of 3.57%.

Acknowledgment

The authors would like to acknowledge the support they received from the National Science and Engineering Research Council of Canada and Ryerson University, which made this research possible.

Table of Contents

| | |
|--|-----|
| Abstract | iii |
| List of Figures | vii |
| List of Tables | ix |
| List of Equations | x |
| 1 Introduction | 1 |
| 1.1 Experimental | 1 |
| 1.2 Numerical | 7 |
| 2 Experimental Setup..... | 12 |
| 2.1 Experimental Apparatus and Procedure | 12 |
| 2.2 Experimental Uncertainties | 14 |
| 3 Finite Element Formulations and Mesh Sensitivity | 16 |
| 3.1 Finite Element Formulations | 16 |
| 3.2 Mesh Sensitivity | 20 |
| 4 Results and Discussion | 23 |
| 4.1 The Effects of Heat Flux | 23 |
| 4.2 The Effects of Channels | 35 |
| 4.3 The Effects of Concentration | 37 |
| 4.4 The Effects of Flow Rate | 40 |
| 4.5 The Effects of Permeability..... | 42 |
| 4.6 The Rate of Removal of Thermal Energy | 43 |
| 4.7 The Effects of Pressure Loss on Pumping Power | 44 |
| 5 Conclusion and Future Work..... | 46 |
| 5.1 Conclusion..... | 46 |
| 5.2 Future Work | 47 |

References..... 48

List of Figures

| | |
|--|----|
| Figure 1 (a)Two-Channels Test Block with 10 PPI Insert and (b) Two-Channels Test Block Dimensions [30]..... | 12 |
| Figure 2 (a)Three-Channels Test Block with 20 PPI Insert and (b) Three-Channels Test Block Dimensions [30]..... | 13 |
| Figure 3 Experimental Apparatus [30] | 14 |
| Figure 4 Two-Channels Numerical Model | 16 |
| Figure 5 The Mesh Sensitivity Data | 21 |
| Figure 6 Three-Channels Finite Element Model | 22 |
| Figure 7 Varied Heat Flux Temperature Distribution at Constant Flow Rate (a) Test 1-3, (b) Test 4-6 and (c) Test 7-9..... | 24 |
| Figure 8 Varied Heat Flux Temperature Distribution at Constant Flow Rate (a) Test 1-3, (b) Test 4-6 and (c) Test 7-9..... | 26 |
| Figure 9 Varied Heat Flux Temperature Distribution at Constant Flow Rate (a) Test 1-3, (b) Test 4-6 and (c) Test 7-9..... | 28 |
| Figure 10 Varied Heat Flux Temperature Distribution at Constant Flow Rate (a) Test 1-3, (b) Test 4-6 and (c) Test 7-9..... | 30 |
| Figure 11 Varied Heat Flux Temperature Distribution at Constant Flow Rate (a) Test 1-3, (b) Test 4-6 and (c) Test 7-9..... | 32 |
| Figure 12 Varied Heat Flux Temperature Distribution at Constant Flow Rate (a) Test 1-3, (b) Test 4-6 and (c) Test 7-9..... | 34 |
| Figure 13 Two-Channels versus Three-Channels Temperature Distribution for Test 7, Test 8 and Test 9..... | 36 |
| Figure 14 Two-Channels versus Three-Channels Temperature Distribution for Test 7, Test 8 and Test 9..... | 37 |
| Figure 15 Nanofluid versus Distilled Water with Temperature Distribution for Test 5 and Test 6 | 38 |
| Figure 16 Nanofluid versus Distilled Water with Temperature Distribution for Test 7, Test 8 and Test 9..... | 39 |
| Figure 17 Nanofluid versus Distilled Water with Temperature Distribution for Test 7, Test 8 and Test 9..... | 40 |

| | |
|--|----|
| Figure 18 The Effects of Flow Rates on the Temperature Distribution for Test 1, Test 4 and Test 7..... | 41 |
| Figure 19 The Effects of Permeability on Temperature Distribution for Test 7 to 9 | 42 |
| Figure 20 Average Nusselt Number for the Six Cases | 43 |
| Figure 21 Pressure Lose for the Six Cases..... | 44 |

List of Tables

| | |
|--|----|
| Table 1 Thermo-physical Properties of Nanofluid with 0.6% Alumina and Distilled Water [1] [2] [3]..... | 17 |
| Table 2 The Mesh Sensitivity Data..... | 20 |

List of Equations

| | |
|---|----|
| Equation 1 Taylor Method with the Nusselt Number | 15 |
| Equation 2 Non-dimensional Naiver-Stokes momentum equation in the X-direction | 18 |
| Equation 3 Non-dimensional momentum equation in the Y-direction | 18 |
| Equation 4 Non-dimensional Naiver-Stokes momentum equation in the Z-direction | 18 |
| Equation 5 Non-dimensional continuity equation | 18 |
| Equation 6 Non-dimensional energy equation for fluid domain | 19 |
| Equation 7 Non-dimensional Darcy-Brinkman momentum equation in the X-direction..... | 19 |
| Equation 8 Non-dimensional Darcy-Brinkman momentum equation in the Y-direction..... | 19 |
| Equation 9 Non-dimensional Darcy-Brinkman momentum equation in the Z-direction | 19 |
| Equation 10 Non-dimensional energy equation for the saturated porous material domain..... | 19 |

1 Introduction

The processing power of electronics is increasing. This means that more thermal energy is produced, which in turns increases the demand of the removal of the thermal energy. Micro-porous channels with nanofluid can be used to efficiently remove the excess heat. This section will explore experimental and numerical studies of previous research.

1.1 Experimental

The first work that is to be mentioned is the work of Ho et al. The nanofluid that was used for the studies that will be discussed was Al_2O_3 [1] [2] [3]. One of Ho et al experiments investigated how natural convection interacts with Al_2O_3 in vertical square enclosures [1]. Three different enclosures where used: the changing factors where the height, depth and length [1]. The concentration range and the Raleigh number range used in the experiment were the following: 0.1 vol% to 4 vol% and 6.21×10^5 to 2.56×10^8 , respectively [1]. The results concluded that when the nanoparticles volume ratio was greater than 2 vol%, the heat transfer enhancement was lost: this was the case across the entire Rayleigh number considered [1]. Also, it was found that when the concentration was 0.1 vol%, there was an 18% improvement in heat transfer when compared to only water [1]. Ho et al conducted an experiment that focused on using Al_2O_3 as a forced convective coolant for a copper micro channel heat sink [2]. A micro channel heat sink used was specifically designed for the experiment [2]. It was important to note that the Reynolds number used was between 226 and 1676 [2]. The results concluded that the inclusion of nanofluid improves the heat transfer capabilities of the heat sink, therefore, a larger average heat transfer coefficient [2]. The last study that will be discussed was the comparative experimental study on the heat transfer enhancement of Al_2O_3 versus water in a copper mini channel heat sink [3]. Similar to the previous experiment, a mini channel heat sink was designed for the experiment [3]. It was important to note that the Reynolds number that was used for this experiment was between 133 and 1515 [3]. It was concluded that the addition of nanofluid to the system greatly improved the average heat transfer coefficient when compared to just water [3].

An experiment was conducted by Pourfarzad et al with a copper porous media [4]. The main objective was to study the convective heat transfer enhancement of Al_2O_3 [4]. For this simple

reason, this study was of particular interest because the same nanofluid was used. It was found that there was an enhancement in the convective heat transfer coefficient and Nusselt number which resulted in an increased Reynolds number [4]. The results concluded that 30 pores per inch (PPI) at a concentration of 0.5% gave the best results [4].

The surface charges of the nanoparticles in the carrying fluid can cause agglomeration [5]. Bouguerra et al studied how the pH range of 4.6 to 6.5 effects the dispersibility of nanoparticles in nanofluids; repulsion or attraction will occur [5]. The Mouromtseff number (Mo) was used to determine the heat transfer enhancement of the nanofluid; a larger Mo indicates a higher heat transfer [5]. Bouguerra et al observed that when the well dispersed regime is present, it must be precedent over all the other dispersion regimes [5]. The chain-like agglomeration (CL agg.) regime has the best heat transfer improvement; however, it was best used if the cost of the pumping power was not a priority [5]. The results showed the thermal conductivity improved more than 23% with a concentration of 2% [5]. Also, the viscosity increase does not negatively affect the thermal conductivity enhancement of the CL agg. regime [5].

The behavioral study of nanofluid has been a main topic of research in past years, however, there was been little focus on the critical heat flux. Wang et al conducted an experiment on the critical heat flux of nanofluid [6]. The experimental observation was from a vertical tube and the parameters that were included were the outlet pressure, mass flux, inlet sub-cooling, heating length, and diameter [6]. As well as the type of the nanoparticles and their concentration used [6], which were both typical parameters used in experimental and numerical studies. It was noted that the apparatus included ultrasonic vibration unit, which was used to keep nanoparticles in suspension [6]. In Wang et al found that there was at most a 18% improvement of the critical heat flux of nanofluid boiling [6]. It was found that the nanoparticles used for inlet sub-cooling: Al_2O_3 and AlN , at a concentration of 0.1 vol% and 0.5 vol% had negligible effect in the experiment [6].

In an experimental study performed by Tiwari et al, the purpose was to determine the optimal parameters of the nanofluid needed to have the most effective heat transfer [7]. The parameter that was varied and tuned for optimization was the volume fraction, with the variance between 0 and 3% [7]. The working fluid used was water and the four nanoparticles used were CeO_2 , Al_2O_3 , TiO_2 , and SiO_2 [7]. It was noted that the test section used was a plate heat exchanger [7]. The results concluded that the best concentration for each of the nanoparticles were the following:

CeO₂ at 0.75%, Al₂O₃ at 1%, TiO₂ at 0.75%, and SiO₂ at 1.25% [7]. The previously stated volume concentrations were the optimal results when the flow rate was equal to 3lpm [7]. At the optimal concentrations the heat transfer enhancement resulted in the following values: 35.9%, 26.3%, 24.1%, and 13.9%, respectively [7].

Nazari et al investigated how the addition of water-based graphene oxide nanofluid effects the heat transfer capabilities in pulsating heat pipes (PHPs) [8]. There were four concentrations of the graphene oxide used in the experiment: 0.25, 5, 1, and 1.5 g/lit [8]. The type of PHP used in the experiment was a 2-turn [8]. Also, graphene oxide sheets were added in the PHP to determine if they influence the thermal performance of the PHP [8]. When the concentration of the graphene oxide increases the improving rate of thermal performance (IRTP) decreases [8]. The optimal concentration to use at 10W of constant heat input was 0.25 g/lit, which resulted in more than a 40% reduction in thermal resistance in PHP [8]. The previously stated results were obtained when there were graphene oxide sheets added to the base fluid [8].

The use of nanoparticles to enhance the ability of solar vapor generation was investigated by Wang et al [9]. The material that was selected for the experiment was carbon nanotube that was suspended in water [9]. The desired characteristic of carbon nanotube was that they have high and broadband absorption in the solar spectrum [9]. The experiment will vary different concentrations of the carbon nanotubes, as well as solar intensities [9]. The highest performing results with a concentration of 19.04×10^{-4} vol% and a solar illumination of 10 Sun (1 Sun = 1 kW m⁻²) produced an evaporation rate of 46.8% [9]. It was found, the solar vapor generation performed more efficiently when the water-to-air interface was heated instead of the total working fluid temperature [9]. It was noted that the evaporation rate can increase with higher concentrations of nano carbon tubes or the solar power was intensified [9].

A custom made flat plate solar collector was designed and built for Colangelo et al, which was used to perform a comparative study on distilled water-based nanofluid with Al₂O₃ nanoparticles and distilled water [10]. The experiment used a high concentration of Al₂O₃ nanoparticles: 3 vol% [10]. The flat plate solar collector was specifically designed to reduce the agglomeration of the nanoparticles, which was needed for high concentrations [10]. The results of the experiment proved that Al₂O₃ nanofluid has more effective heat transfer capabilities then distilled water at

high temperatures [10]. As well as there was a 11.7% improvement in the thermal efficiency in the solar collector when Al_2O_3 nanoparticles was used [10].

Some types of solar collectors use a water-based compound for the working fluid. Kim et al conducted an experimental study to see if using Al_2O_3 as the working fluid increases the power production of a U-tube solar collector [11]. The experiment will use a variety of concentrations as well as nanoparticle sizes [11]. To conduct the experiment two U-tube solar collectors were installed with southern exposure at 45° in Gwangju, Korea [11]. One solar collector had Al_2O_3 as the working fluid and the other had water [11]. The most effective combination of particle size, concentration, and flow rate was at 20nm, 1.0 vol%, and 0.047 kg/s, respectively [11]. The performance of Al_2O_3 nanofluid in the previously stated conditions was 24% more efficient than water as the working fluid [11]. It was noted that the efficiency of nanofluid decreased at high concentrations [11].

Gan et al performed an experimental study to harmonies' parameters for the best thermal properties and entropy generation of titanium dioxide nanofluid, which was being used as the working fluid in evacuated tube solar collectors (ETSC) [12]. The carrying fluid used in the experiment was distilled water [12]. The purpose of this journal was to determine the thermal efficiency as well as conduct an entropy analysis of the ETSC [12]. There were three conditions varied for the experiment: volumetric concentration of nanoparticles, amount of surfactant and sonication time [12]. The ETSC experiment was performed at the University of Malaya [12]. The best combination of the varied conditions as mentioned above were 0.50 vol% of titanium oxide nanoparticles, surfactant-to-nanoparticle ratio of 1:1 and having a 10 minutes sonication [12]. The thermal efficiency increase in the ETSC during the previously stated optimal conditions was 7.28% [12]. It was noted that the thermal efficiency increases in parallel to an increasing mass flow rate [12].

Wongcharee et al investigated the applicational use of nanoparticles in swirling impinging jets [13]. The nanoparticle that was selected for the study was CuO, the carrying fluid used was water [13]. To initiate the swirling flow, twisted tap was used and inserted into the swirl generator, it was noted that the twisted tape material was aluminum [13]. There will be three twisted tape insert test sections used in the experiment, the twist ratio was 1.43, 2.86 and 4.28 [13]. The nanoparticles used will be at high concentrations, which were 2 vol%, 3 vol% and 4 vol% . [13]

Also, the ratio for the distance between the jet-to-plate and the nozzle diameter will be varied: 2, 3, and 4 [13]. The experimental results will be compared to water to see if there was improvement or not in heat transfer [13]. The Reynolds number used in the experiment was in the laminar, transition and turbulent region, and the values will be between 1600 to 9400 [13]. It was found that CuO nanoparticle concentration at 2 vol% and 3vol% had better heat transfer performance when compared to water, while 4 vol% performed worse than water [13]. From all the varied parameters the combination that performed the best was when the ratio jet-to-plate spacing to nozzle diameter was equal to 2, twist ratio was 1.43 and the concentration of the CuO was at 2 vol% [13].

Afrand et al in 2016 performed the first experiment on the rheological behavior of Fe₃O₄-Ag/EG [14]. The experiment will vary temperature: 25°C to 50°C, and the concentration of the hybrid nanofluid: 0.0375 vol%, 0.075 vol%, 0.15 vol%, 0.3 vol%, 0.6 vol%, and 1.2 vol% [14]. To determine the viscosity of the hybrid nanofluid for each test, the Brookfield DV-I PRIME digital Viscometer was used [14]. It was noted that the shear rates (12.23-122.3 s⁻¹) were varied during the viscosity measurements [14]. It was revealed that the hybrid nanofluid can behave as either a Newtonian or a non-Newtonian fluid [14]. When the concentration of the hybrid nanofluid was from 0.0375 vol% to 0.3 vol% the fluid was Newtonian [14]. While from a range of 0.6 vol% to 1.2 vol% the fluid was non-Newtonian and was consistent with the power-law model [14]. Also, the non-Newtonian range for the hybrid nanofluid displayed shear-thinning at all variations of the temperature range [14].

Sen et al investigated the maximum amount of nanoparticle concentration allowed in the nanofluid before degrading the electrochemical response [15]. The goal was to also maintain a minimal change in the viscosity [15]. The nanoparticle that was used in this experiment was titania [15]. There were many different measurements taken to determine the changes that have occurred before and after surface modification of the nanoparticles [15]. The main measurements are discussed below. The measurement devices used were a thermal property analyzer and a rotational-type viscometer, which was used to determine the if there were any changes in the thermal characteristics and viscosity of the nanofluid, respectively [15]. Agglomeration was a concern when using high concentration nanoparticles, dynamic light scattering measurements were taken to determine if there was any formation [15]. To determine if the electrochemical properties of

the nanofluid were maintained solid-casted electrodes were evacuated before any after surface modification [15]. The results concluded it was possible to graft organic molecules that have negatively charged sulfonate with a versatile one step procedure onto titania nanoparticles [15]. It was successfully demonstrated that the electrochemical response was maintained more than 78% with a surface-modified titania nanoparticle than without [15]. This enhancement can lead to more efficient electrochemical energy storage [15].

A comparative study was conducted by Cabalerio et al to determine the isobaric specific heat capacity of five unique nanofluids [16]. The nanoparticles that were selected for the experiment were the following: MgO, ZnO and ZrO₂ in pure ethylene glycol and ZnO and ZrO₂ in half and half ethylene glycol and water compound [16]. The nanoparticles will have a maximum mass concentration of 15% [16]. The quasi-isothermal Temperature-Modulated Differential Scanning Calorimetry method was used to evaluate the isobaric specific heat capacity [16]. The temperature range used for the experiment was between 243.15 to 473.15 kelvin [16]. As with most experimental and numerical studies the results obtained for the five nanoparticles and base fluid were validated with other journals [16]. From the results, an equation was developed to determine the likeness between the specific heat values of nanofluids with respect to the base fluid, nanoparticles, and the nanoparticle concentration [16].

Cabalerio et al conducted an experimental study to determine the stability and thermophysical behavior of nanofluids that were created for dispersions of sulfonic acid-functionalized graphene nanoplates [17]. The carrying fluid that was used for the nanoparticles was a combination of ethylene glycol and water, the mass ratio used was 10:90% [17]. There were three devices used to analyze the thermal conductivity, rheological behavior and the density of the prepared nanofluid samples [17]. The three devices used were TPS 2500 S Hot Disk Thermal Analyzer, AR G2 magnetic bearing rotational rheometer, and Anton Paar DMA 4500 vibrating U-tube densimeter, respectively [17]. The results showed that the temperature was not directly affected when the thermal conductivity enhancement was less than or equal to 5% [17]. At the same enhancement level, the rheological results showed that the nanofluid behaved like a Newtonian fluid [17].

1.2 Numerical

A semi-annular enclosure was widely used in engineering applications, for example, solar collectors, cooling of electronic components, heat exchangers, and nuclear reactors [18]. Bezi et al conducted a numerical simulation to broaden the scope of how nanofluids with varying nanoparticles effected the natural convection and entropy generation within an inclined half annulus, which was heated from top surface [18]. The simulation used a water based nanofluid with different types of nanoparticles: Au, Ag, Cu, and CuO [18]. Bezi et al used a custom FORTRAN code, which was based on a finite volume method simulation to conduct the study [18]. The results concluded that the median entropy generation from heat transfer was enhanced by increasing the volume fraction of the nanoparticles and the Rayleigh number [18].

There were many different research topics on mixed convection. In some engineering applications, the surfaces can be uneven, for example the surface could be wavy [19]. Further investigation on the effect of nanofluid on thick wavy wall was conducted by Pal et al [19]. Pal et al main focus was to perform an analysis on how the behavior of the conduction on the outside of the thick wavy heated wall, as well as the conjugate heat transfer, which had mixed convection, influences the Cu-water nanofluid [19]. The approach that Pat et al used was a finite volume method that implements a large range of the Richardson number, nanoparticle volume fraction, wave amplitude, wave number, and wall-to-fluid conductivity ratio with a varying Reynolds number [19]. The results were in agreement with the scientific community that the addition of nanoparticles increases the rate of heat transfer in the working fluid [19]. Finally, the wavy wall was more effective when the conductivity of the solid and fluid were within the same magnitude [19].

Sheremet et al used Darcy and Buongiorno's model to analytically model the effects of mixed convection with porous media and nanofluid [20]. The nanofluid was subjected to suction or injection within a square porous cavity [20]. The nanofluid used for the numerical study was water-based, there were no specifications on the type of nanoparticles used in the simulation [20]. The equations that were developed were dimensionless and based on the stream function, temperature and the nanoparticles volume fraction [20]. The governing equations were solved using a code that was based on the finite difference method, which was developed locally [20]. It was found that along the hot wall the flow of the nanofluid would increase when there was a larger

Rayleigh number [20]. Also, the larger Rayleigh number impacts the thickness of the thermal boundary layer; i.e. it becomes smaller, and the nanoparticles gather in the upper corners of the model, which leads to a higher concentration in the area [20]. It was shown that having a larger Reynolds number increases the cooling capability of the nanofluid in the cavity, as well as the escalation of thermophoresis of the nanoparticles from the hot to cold wall [20].

Finding the optimal wall thickness was important because it minimizes the weight and cost of a design. Kumar et al conducted a numerical study using Matlab bvp4c to study the behavior of the hydromagnetic boundary layer of nanofluid, which was flowing across a stretching sheet [21]. Also, multiple iterations were conducted with a varying wall thicknesses of the stretching sheet [21]. The heat flux model that was mainly used was the Cattaneo-Christov heat flux model [21]. Kumar et al main observation was that the velocity of the fluid increased with a larger wall thickness and with a velocity exponent parameter greater than one [21]. It was noted that a smaller wall thickness results a decreasing velocity when the velocity exponent parameter was less than one [21].

Nanoparticles increase the pumping power required for a system. Therefore, there needs to be a balance between the enhanced heat transfer capabilities of nanoparticles and the extra cost of the pumping power required. There have been studies that investigate the optimization of the thermal characteristic improvements of nanoparticles and porous media, which was another common approach of enhanced heat transfer. A numerical study by Siavashi et al focuses on utilizing the full potential of the thermal characteristic enhancements of gradient and multi-layered porous media (GPM and MLPM, respectively) [22]. There will be multiple configurations of the GPM and MLPM numerically test to find the optimal properties: porosity and particle size or permeability [22]. The software ANSYS-FLUENT will model the fluid flow through a pipe that was filled with GPM and MLPM [22]. Each layer can have independent properties [22]. There were two methods implemented, porous media insert and nanofluid (nanoparticles plus the base fluid used) [22]. The porous media insert method consisted of two different cases. The first was that the porosity was kept constant while the particles size or permeability changed in size, there were several combinations used [22]. The second was that the porosity varied, and the particle size was kept constant [22]. The results for case 1 performance evaluation criteria was 0.845, while case two was 0.789 [22]. Also, the performance evaluation criteria can be improved to around

three times by adding a 5% concentration of nanofluid composed of water and alumina nanoparticles [22].

Mwesigye et al conducted a theoretical analysis of the heat transfer enhancement of using high concentration nanofluid for the working fluid for a parabolic trough solar collector [23]. The nanofluid that was selected was Cu-Therminol[®]VP-1 and high concentrations will be used [23]. The mathematical method used was the Monte-Carlo ray tracing and computational fluid dynamic procedure [23]. To find the heat flux profile of the receiver absorber tube the Monte-Carlo tracing ray procedure was used, which was then paired with the computational fluid dynamics procedure to evaluate the heat transfer enhancement of the receiver [23]. The theoretical analysis concluded at the highest concentration of nanoparticles, 6%, there was at most a 12.5% thermal efficiency enhancement [23]. It was found that only for some ranges of the Reynolds number with the nanoparticles there was an improvement in the thermodynamic performance of the reservoir [23]. It was noted that the entropy generation minimization method was used to determine the results stated previously [23].

A numerical study on the interaction of nanofluid flow with an asymmetric wall and how effective the heat transfer was conducted by Zhu et al [24]. The concepts that were investigated in detail were the wall heat fluxes with nonlinear velocity slip [24]. The mathematical analysis was developed using the Local Thermal Non-Equilibrium model as well as the second-order slip model was implemented to consider the boundary conditions [24]. The nanoparticles used in the analysis were Cu and Fe₃O₄, both nanoparticles use water as the carrying fluid [24]. The results showed that the Nusselt number increases during the first velocity slip, while during the second slip the opposite effect occurs [24]. The performance of the heat transfer was higher when the nanoparticle concentration was increased [24]. Also, the heat transfer performance was higher when the Hartmann number was larger [24]. There was no surprise when there was a more efficient heat transfer enhancement for the bottom wall [24]. It was noted that the results found were compared with other journals and were in good agreement [24].

In this case, instead of a conventional shape, Toghraie et al performed numerical study on L shaped micro-porous ribs [25]. The varying parameters that were focused on were the volume fraction and Reynolds number [25]. The nanofluid that was used was CuO with a varying concentration of 2 to 4% [25]. The flow regime that was selected for the numerical study was laminar [25]. It was

found that the nanofluid does not contribute to any enhancement in heat transfer with this shape [25]. Shown in the results, when Reynolds number was 1200, there was a 42% increase in heat transfer [25]. While at a Reynolds number of 100, the increase in heat transfer was 25% [25].

Siavashi et al performed a numerical study regarding the performance of natural convection with Cu-water nanofluid and porous fins [26]. The porous fins were located on the hot wall of the numerical model [26]. The numerical model was designed in 2-phases: nanofluid and the Darcy-Brinkman-Forchheimer for the porous region [26]. There were three parameters that were varied for the numerical study: Raleigh number, Darcy number and nanoparticle volume fraction [26]. The range used were 10⁴ to 10⁶, 10⁻¹ to 10⁻⁴ and 0 to 0.04, respectively [26]. The results showed that with a larger Darcy number, the heat transfer qualities were increased when porous fins were used [26]. While, a reduction in the Darcy's number can reduce the effects of convection and Nusselt number [26]. The results showed that the improvement in heat transfer was better when the nanoparticle volume fraction was small, compared to larger amounts [26]. In addition, the entropy declined in parallel to the addition of more fins, while the performance coefficient improved when porous fins were used: this occurred in many of the numerical cases [26]. Finally, when pure fluids were used in the numerical cases, the performance coefficient was improved when compared to nanofluids at a smaller Raleigh number [26]. It was noted that with the larger Raleigh number the reverse results were seen [26].

Guo et al conducted a numerical study on how the thermal and hydraulic properties behaved in a micro fin heat sink when using ZnO nanofluid: water was the carrying fluid [27]. The two models that were used for the study were the static and dynamic single phase [27]. It was important to note that the Brownian motion effect was implemented in the dynamic single-phase model [27]. The parameter that was compared for the static and dynamic model was the heat transfer coefficient the enhancement range was between 16.6% to 23.8% and 25.6% to 38.3%, respectively [27] It was noted that the previous values stated had a Reynolds number range of 85 to 595 and at a concentration of 3% of ZnO [27]. The maximum heat transfer was for the dynamic single-phase model at a concentration of 3%, the value was 34.9 [27].

The work of Bayomy et al was presented below [28] [29]. The experimental and numerical study modeled a heat sink and aluminum foam metal; they both have identical dimensions to an intel core i7 processor [28] [29]. The first study that will be discussed was Bayomy et al numerical and

experimental study on an aluminum foam metal block with water as the working fluid [28]. The experimental and numerical study was assumed to be steady state and was in the non-Darcy flow regime, which has a Reynolds number range of 297 to 1353 [28]. The heater that was used had a heat flux range of 8.5 to 13.8 W/cm² [28]. The purpose of this study was to observe the thermal heat development and thermal entry length when using an aluminum foam block [28]. The results found that at higher Reynolds number there was a longer thermal entry length, while the opposite occurs with a smaller Reynolds number [28]. Also, the results indicated that the local Nusselt number was highly dependent on the Reynolds number in the fully developed region [28]. Finally, when the numerical and experimental results were compared with the local Nusselt number and the local temperature the maximum relative error was 0.83% and 0.43%, respectively [28]. The second study that will be discussed was Bayomy et al work on the heat transfer abilities of ERG aluminum foam block and γ -Al₂O₃ nanofluid with water [29]. Same as the previously discussed study, the experimental and numerical cases were assumed to be steady state and in the non-Darcy flow regime, however, the Reynolds number range was 210 to 631 [29]. In this study the concentration range that was used was between 0.1 vol% to 0.6 vol% [29]. It was important to note that all results were compared with a channel without foam metal and nanofluid; meaning water [29]. It was found that when the foam metal and nanofluid were added, the average Nusselt number had an enhancement factor of 20% [29]. The optimal enhancement was shown at a concentration of 0.2 vol%, then the enhancement trend rapidly decreased at 0.3 vol%, however, there was a gradual increase until 0.6 vol% [29]. At 0.2 vol% the average enhancement percentage of the Nusselt number compared to water was 37% and 28% at a Reynolds number of 601.3 and 210, respectively [29]. The experimental and numerical results had a max relative error of 3% and 2%, when comparing the local Nusselt number and local temperature, respectively [29].

Following, there are four main sections. The Experimental Setup section will highlight the main components of the apparatus, materials used and the experiment uncertainties. The Finite Element Formulations and Mesh Sensitivity section will discuss the parameters and formulas used to model the simulation and analyze the mesh sensitivity test. The Results and Discussion will analyze the temperature distribution, average Nusselt number and pressure losses for the case studies used. Finally, the Conclusion section will discuss the main findings in the experimental and numerical study.

2 Experimental Setup

The experimental setup and numerical modelling section will discuss the experimental apparatus and procedure as well as experimental uncertainties.

2.1 Experimental Apparatus and Procedure

The experimental apparatus is designed to observe the heat transfer enhancement potential of micro-porous channels, when using nanofluid or distilled water. The flow rate is a varying parameter in the experiment, which are 0.1, 0.2 and 0.3 USGPM. The test section is designed to have interchangeable test blocks. The permeability selected for the study are 10 and 20 pores per inch (PPI). There are two different test blocks used in the study, which are shown in Figure 1 and Figure 2 below. Details of each test block is discussed below. Also, each test block has 10 and 20 PPI inserts.

The first test block discussed is shown in Figure 1. Figure 1 (a) shows the two-channels test block used in the experiment, the 10 PPI inserts are depicted in the figure. There are two channels which have a uniform spacing of 7.5 mm. The length, width and depth are the following: $37.5 \times 37.5 \times 12.7$ mm. The dimensions are shown in Figure 1 (b).

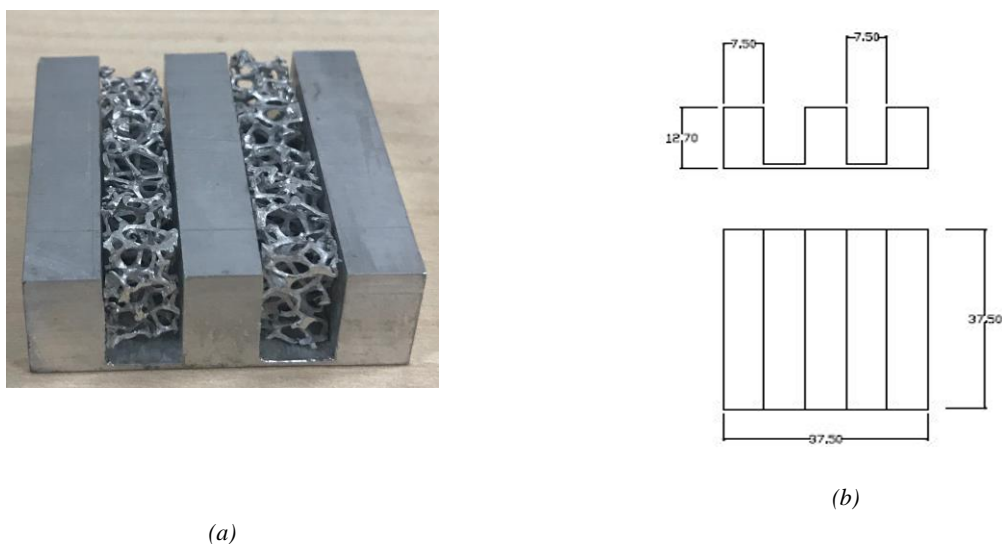


Figure 1 (a) Two-Channels Test Block with 10 PPI Insert and (b) Two-Channels Test Block Dimensions [30]

The second test block discussed is shown in Figure 2. Figure 2 (a) shows the three-channels test block used in the experiment that has the 20 PPI inserts. There are three-channels which have a uniform spacing of 5.35 mm. The length, width and depth are the following: $37.5 \times 37.5 \times 12.7$ mm. The dimensions are shown in Figure 2 (b).

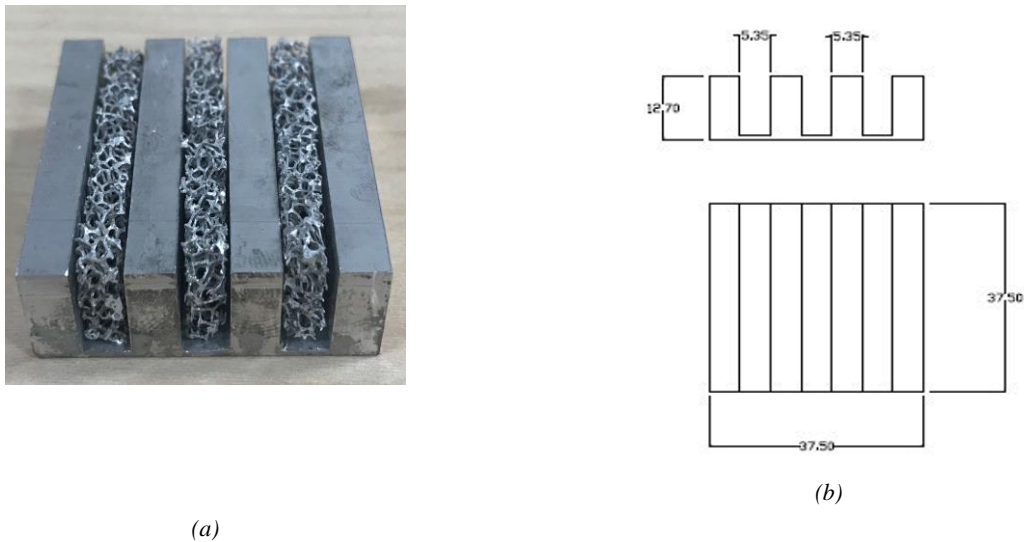


Figure 2 (a) Three-Channels Test Block with 20 PPI Insert and (b) Three-Channels Test Block Dimensions [30]

It is important to note that the dimensions of the test blocks model an intel core i7 processor. Shown in Figure 3 is the experimental apparatus used. The test section has a heater built in and has the following dimensions: $37.5 \times 37.5 \times 12.7$ mm, which are the same as a core intel i7 processor. The two or three channels test block is inserted into the test section. There are ten type (T) thermocouples used in the test section: one is used for both inlet and outlet, and eight for measuring the change in temperature across the heat sink. The readings that are collected are used to calculate the heat transfer enhancement. The temperature of the fluid is controlled by a heat exchange, which is used to cool the fluid after the heat sink. The chiller connected to the heat exchanger is kept at a constant temperature of 4°C . Multiple runs of the experiment were conducted with varying heat fluxes, test blocks and working fluid.

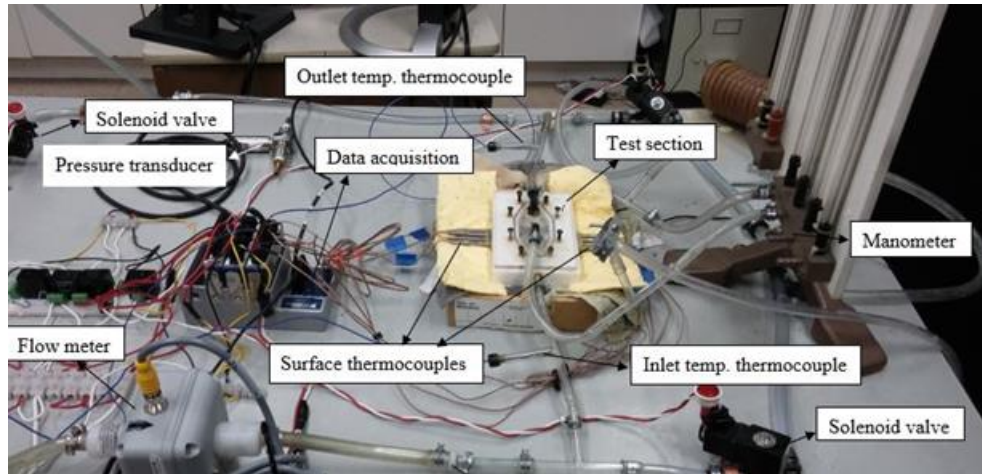


Figure 3 Experimental Apparatus [30]

There are two working fluids used for the experiment: alumina nanofluid (Al_2O_3) and distilled water. The alumina nanofluid is supplied by MK Nano [31]. The concentration that is used is 0.6%. The particle size of the alumina nanofluid is 50 nm. To achieve the desired concentration, distilled water is added as a carrying fluid to the alumina nanofluid. The volumetric concentration method is used. The alumina nanofluid is re-agitated to prevent agglomeration effects that can occur. The second working fluid used is distilled water. Distilled water is used for a base line for the experiment. The aluminum foam metal block inserts (10 and 20 PPI) are supplied by ERG Aerospace [32]

A summary of the parameters used in the experiment are the following: two and three channel test blocks, flow rates of 0.1, 0.2 and 0.3 USGPM, 10 and 20 PPI inserts, and nanofluid with 0.6% alumina and distilled water. The term nanofluid will be used to describe the nanofluid with 0.6% alumina used in the experimental and numerical cases.

2.2 Experimental Uncertainties

When conducting an experiment, there are always uncertainties. In this study the uncertainties come from the thermocouples, which are used to collect the temperature distribution, the flow rate and the heat flux. There are uncertainties for the pressure loss, however, the pressure loss data will come from the Numerical study. Thus, not part of the experimental uncertainties. The

uncertainties that are found for the thermocouples and flow rate are the following: 0.75% and 0.44%, respectively. These values are from the calibration conducted by Bayomy et al [28]. The heat flux uncertainties are derived from the input current, the input voltage, and the thickness of the thermal paste, which is used in the test section. It is important to note that the current and voltage are partially influenced by the wall outlet, because it is the main power source used for the experiment. It is found that the current and voltage had an error of 2% and 1.7%, respectively. These are both approximations that are seen in the measurements taken during the experiment. The uncertainties are calculated with the Taylor method. The Taylor method is used to calculate the amassed error that occurs when using multiple experimental parameters that have uncertainties. The Nusselt number used to determine the rate of removal of thermal energy has such error. An example of the Taylor method using the Nusselt number is shown below in .

$$\delta Nu_x = \sqrt{\left(\frac{\partial Nu_x}{\partial x} \cdot \delta x\right)^2 + \dots + \left(\frac{\partial Nu_x}{\partial y} \cdot \delta y\right)^2 + \dots + \left(\frac{\partial Nu_x}{\partial z} \cdot \delta z\right)^2} \quad \text{Equation 1}$$

The terms x, y and z terms are place holders for the other variables used to calculate the Nusselt number, which are the temperature and the velocity of the fluid.

3 Finite Element Formulations and Mesh Sensitivity

Numerical modeling is conducted to validate the accuracy of the experiment. The finite element formulations used in COMSOL is discussed below. As well a mesh sensitivity test is conducted to confirm the number of elements used provides an accurate representation of the temperature distribution.

3.1 Finite Element Formulations

The simulation software used in the present study is COMSOL Multiphysics [33]. There are three domains to consider for the model: solid, fluid, and saturated porous material. The domains are shown below in Figure 4 and the domains are labeled with a number.

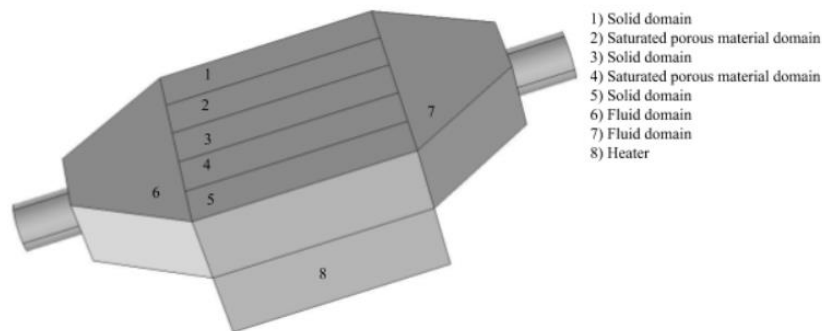


Figure 4 Two-Channels Numerical Model

The numerical model represented in Figure 4 is used for the two-channels simulations. The solid domains are numbered 1, 3 and 5, this represents the solid portion of the test block, meaning two channels. The solid domain indicates that there is a boundary at the wall, therefore, are the walls for the channels. The saturated porous media, labelled as 2 and 4 in Figure 4, is the foam metal with fluid. The permeability of the foam is changed within the parameters of the simulation software. The permeability used for 10 and 20 PPI are 6.8612×10^{-7} and 4.13223×10^{-7} , respectively. The fluid domains are numbered 6 and 7, which is the location of the inlet and outlet. The heater indicated with number 8 is an evenly distributed constant heat flux applied to the test

block. The numerical model is assumed to be steady state; hence, a stationary solver is used. The local thermal equilibrium (LTE) model is applied as well, because it is assumed that the fluid, being the alumina nanofluid or distilled water, the test block, and foam metal inserts where at the same temperature. There are six other assumptions made for the numerical model: fixed flow rate, constant temperature, open thermal and fluid boundary, applied heat flux, non-slip at the walls, and all the outside boundaries are thermally insulated. The experimental results are used to input the values for the heat flux and inlet conditions. All the remaining initial conditions are from the time of the experimental set up. Table 1 shown below outlines the thermo physical properties of nanofluid with 0.6% alumina and distilled water used in the numerical modeling. It is important to note that the three-channels numerical model has the same conditions applied as the two-channels model.

Table 1 Thermo-physical Properties of Nanofluid with 0.6% Alumina and Distilled Water [1] [2] [3]

| C_v (%) | μ_{nf} (kg/ms) | ρ (kg/m ³) | $C_{p_{nf}}$ (J/kgK) | k_{nf} (W/mK) |
|--------------|-----------------------|--------------------------------|-------------------------|--------------------|
| 0 | 0.001002 | 998.2 | 4182 | 0.613 |
| 0.6 | 0.00104 | 1013.811 | 4109.19825 | 0.624262 |

The governing equations will be discussed in two sections: fluid flow and heat transfer. First, the following assumptions are assumed for the equations: incompressible fluid, Newtonian, the porosity of the metal foam is uniform, and LTE. The Naiver-Stokes equation is used to model the fluid flow in the fluid domain, and the Darcy-Brinkman equation is used to model the fluid flow in the saturated porous material domain. The Naiver-Stokes equation and energy equation are discussed first and are formulated into non-dimensional terms with the following relationships.

$$U = \frac{u}{U_o}, V = \frac{v}{U_o}, W = \frac{w}{U_o}, X = \frac{x}{De}, Y = \frac{y}{De}, Z = \frac{z}{De}, \theta = \frac{(T - T_{in})}{q'' \cdot \frac{De}{k_{eff}}}, \text{ and } P = \frac{pDe}{\mu U}$$

In this case, D_e is the hydraulic diameter and U_o is the velocity at the inlet. The momentum equations for X direction is shown below. It is noted that the X, Y, and Z momentum equations are represented as non-dimensionless.

$$Re \left(U \frac{\partial U}{\partial X} + V \frac{\partial U}{\partial Y} + W \frac{\partial U}{\partial Z} \right) = \frac{\partial P}{\partial X} + \left(\frac{\partial^2 U}{\partial X^2} + \frac{\partial^2 U}{\partial Y^2} + \frac{\partial^2 U}{\partial Z^2} \right) \quad \text{Equation 2}$$

The velocity component in the X direction is represented by the term U. The Reynolds number, Re, is equal to $\frac{U_o d}{\nu}$. With U_o being the inlet velocity, d is the diameter at the inlet, and the kinematic viscosity is ν . The next equation is the Y-momentum.

$$Re \left(U \frac{\partial V}{\partial X} + V \frac{\partial V}{\partial Y} + W \frac{\partial V}{\partial Z} \right) = \frac{\partial P}{\partial Y} + \left(\frac{\partial^2 V}{\partial X^2} + \frac{\partial^2 V}{\partial Y^2} + \frac{\partial^2 V}{\partial Z^2} \right) + Ra(\theta) \quad \text{Equation 3}$$

The terms V is the velocity in the Y-direction. The Rayleigh number (Ra) is used to represent lower flow rates and is related to the non-dimensionless temperature θ . The next equation is the Z- momentum.

$$Re \left(U \frac{\partial W}{\partial X} + V \frac{\partial W}{\partial Y} + W \frac{\partial W}{\partial Z} \right) = \frac{\partial P}{\partial Z} + \left(\frac{\partial^2 W}{\partial X^2} + \frac{\partial^2 W}{\partial Y^2} + \frac{\partial^2 W}{\partial Z^2} \right) \quad \text{Equation 4}$$

The velocity in the Z-direction is depicted by the term W. The continuity equation is used to relate the momentum equation for Newtonian fluids and is shown below.

$$\left(\frac{\partial U}{\partial X} + \frac{\partial V}{\partial Y} + \frac{\partial W}{\partial Z} \right) = 0 \quad \text{Equation 5}$$

The energy equation used is the following:

$$\text{RePr} \left(U \frac{\partial \theta}{\partial X} + V \frac{\partial \theta}{\partial Y} + W \frac{\partial \theta}{\partial Z} \right) = \left(\frac{\partial^2 \theta}{\partial X^2} + \frac{\partial^2 \theta}{\partial Y^2} + \frac{\partial^2 \theta}{\partial Z^2} \right) \quad \text{Equation 6}$$

Where, Pr is the term for the Prandtl number and has the following equation: $\frac{C_p \mu}{k}$. The specific heat is C_p , μ is the viscosity, and k is the fluid conductivity. The next set of equations discussed are the Darcy-Brinkman equations and energy equation. The formulas are in the X, Y, and Z direction, respectively.

$$\frac{1}{\text{Da}} U = -\frac{\partial P}{\partial X} + \left(\frac{\partial^2 U}{\partial X^2} + \frac{\partial^2 U}{\partial Y^2} + \frac{\partial^2 U}{\partial Z^2} \right) \quad \text{Equation 7}$$

$$\frac{1}{\text{Da}} V = -\frac{\partial P}{\partial Y} + \left(\frac{\partial^2 V}{\partial X^2} + \frac{\partial^2 V}{\partial Y^2} + \frac{\partial^2 V}{\partial Z^2} \right) + \text{Ra}\theta \quad \text{Equation 8}$$

$$\frac{1}{\text{Da}} W = -\frac{\partial P}{\partial Z} + \left(\frac{\partial^2 W}{\partial X^2} + \frac{\partial^2 W}{\partial Y^2} + \frac{\partial^2 W}{\partial Z^2} \right) \quad \text{Equation 9}$$

The term Da in all three equations is Darcy number. The last equation is the energy equation.

$$\text{RePr} \frac{k}{k_{eff}} \left(U \frac{\partial \theta}{\partial X} + V \frac{\partial \theta}{\partial Y} + W \frac{\partial \theta}{\partial Z} \right) = \left(\frac{\partial^2 \theta}{\partial X^2} + \frac{\partial^2 \theta}{\partial Y^2} + \frac{\partial^2 \theta}{\partial Z^2} \right) \quad \text{Equation 10}$$

Where, k_{eff} is the effective conductivity.

3.2 Mesh Sensitivity

The mesh sensitivity is used to verify the mesh used in the numerical modelling. This means that the number of elements used must be able to give an accurate representation of the temperature distribution. The mesh sensitivity analysis is conducted by selecting one case, which is the 10 PPI with nanofluid and three-channels case Test 1. The desired flow rate is 0.1 USGPM, because it takes less computational time to run. Shown below in Table 2 is the data that is collected for the mesh sensitivity analysis.

Table 2 The Mesh Sensitivity Data

| Element Size | Time (s) | Number of Elements | Maximum Temperature (C°) |
|------------------|----------|--------------------|--------------------------|
| Extremely Coarse | 11 | 8833 | 32.45 |
| Extra Coarse | 20 | 22814 | 33.79 |
| Coarser | 29 | 42208 | 34.07 |
| Coarse | 61 | 109730 | 34.50 |
| Normal | 95 | 213721 | 34.56 |
| Fine | 207 | 489815 | 34.60 |
| Finer | 506 | 1284002 | 34.69 |
| Extra Fine | 6020 | 6309741 | 34.83 |

In Table 2, there is no extremely fine element size, because the computational time is estimated to be around eight hours, which is not possible with the computer that is being used for the numerical modeling. It is important to note that the computational time is dependent on the processing power of the computer that is being used. In this case an 8th generation i7 intel core 3.6 GHz processor is used. The results of Table 2 are represented below in Figure 5.

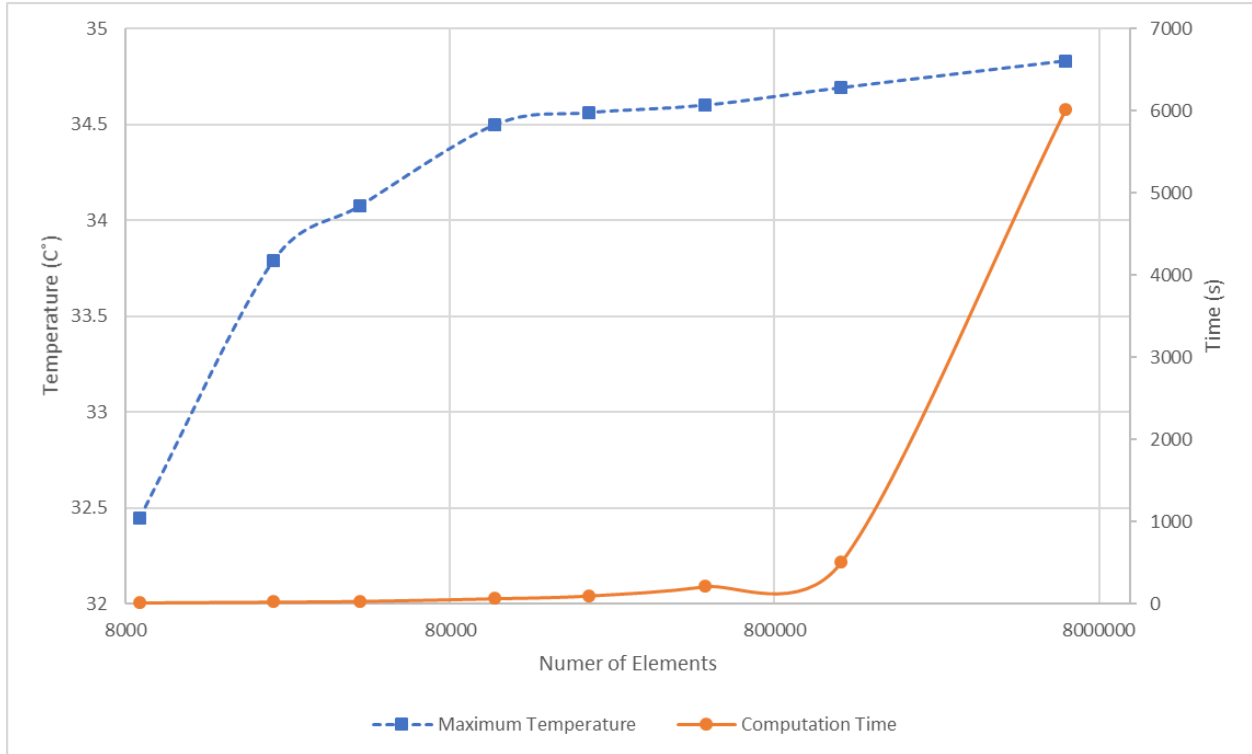


Figure 5 The Mesh Sensitivity Data

The element size has negligible effect when a coarse mesh is used. The computational time for an extra fine size is 6020s, which is an unrealistic time for running multiple simulations. As well as the fact that the level of accuracy associated with the extra fine mesh is not needed for this study. The element size that is selected for all the cases is normal. The reason is the computational time is reasonable with the number of elements. Shown in Figure 6, is an illustration of the mesh that is used for the modeling.

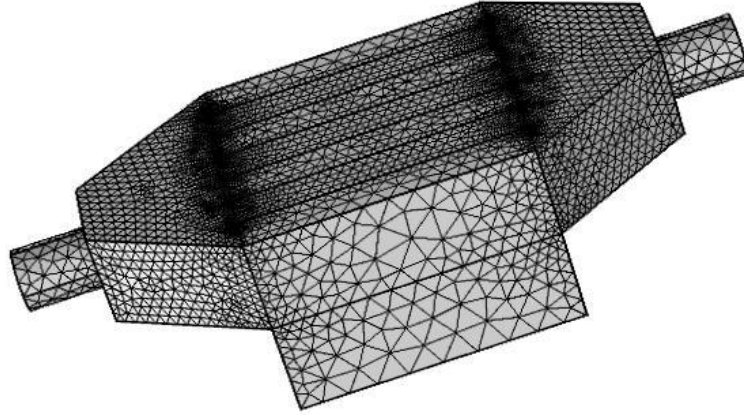


Figure 6 Three-Channels Finite Element Model

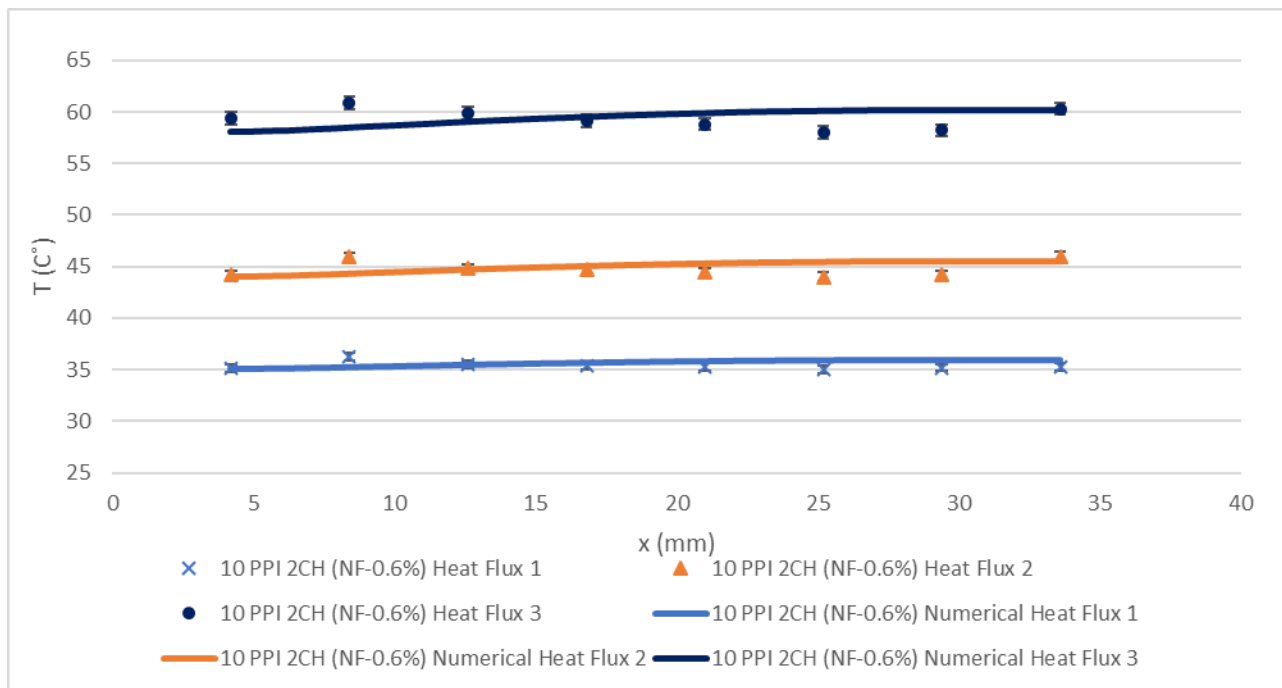
Figure 6 is the three-channels finite element model that is used. The shape that is used in the mesh for Figure 6 is a triangle, which is a typical shape to used in finite element modeling. The number of elements used is 213721. As well as the minimum element quality is 0.2012. The numerical model is considered converged when the error is 10^{-6} .

4 Results and Discussion

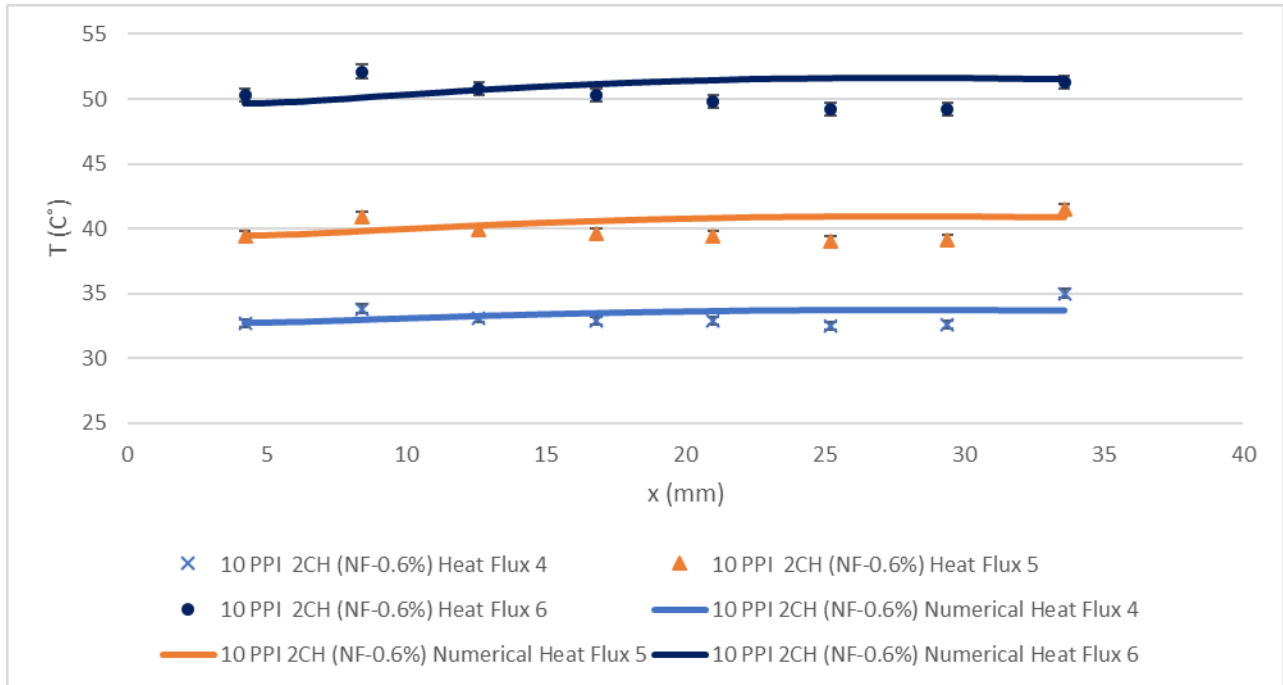
The results and discussion section will analyze the effects of heat flux, concentration, number of channels, and permeability on the temperature distribution. As well the average Nusselt number and pressure loss will be discussed.

4.1 The Effects of Heat Flux

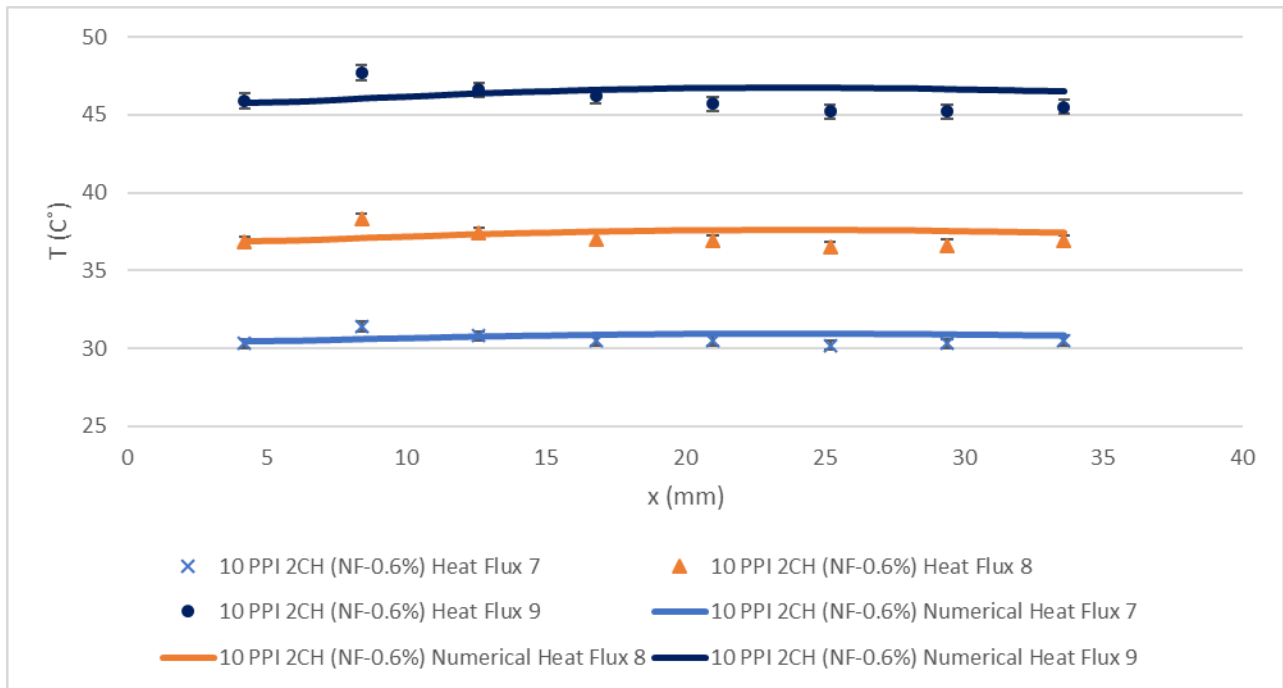
The results that are discussed will analyze the experimental and numerical cases. There will be six cases discussed with varying parameters. Each case has nine tests. The flow rates associated Test 1 to 3, Test 4 to 6 and Test 7 to 9 are the following: 0.1, 0.2 and 0.3 USPGM, respectively. The first case discussed is 10 PPI with 0.6% alumina and two-channels, which is shown below in Figure 7.



(a)



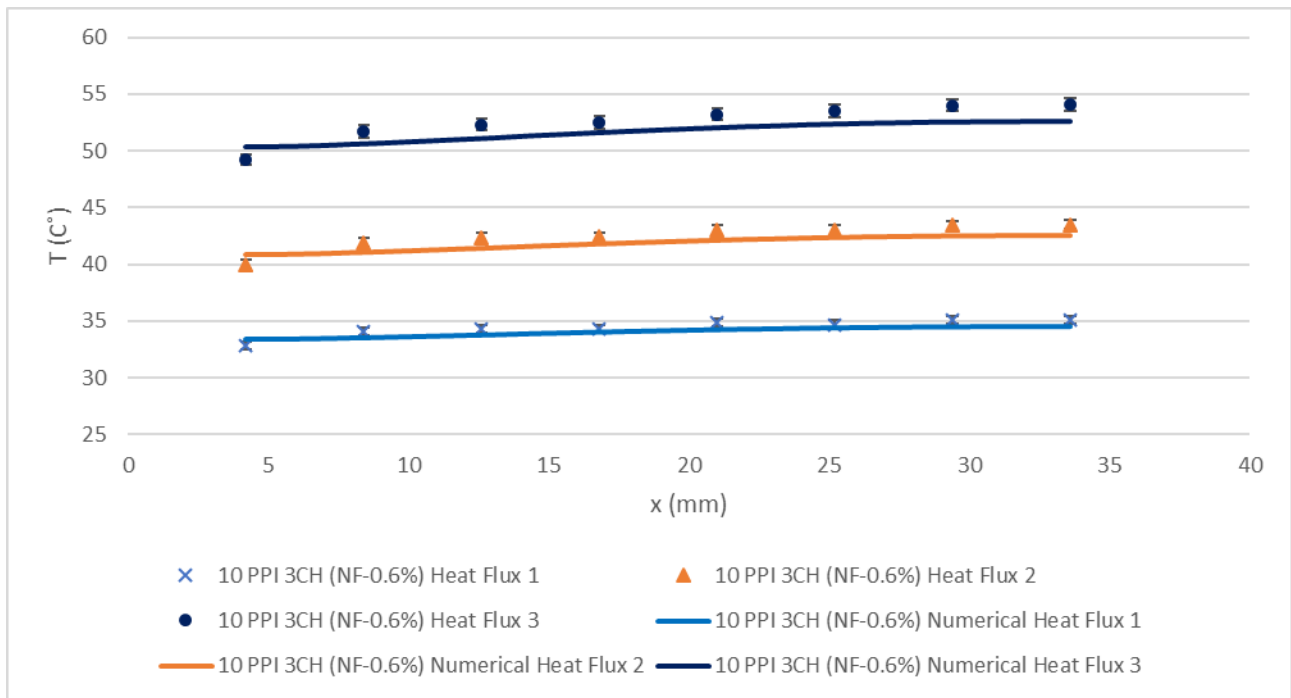
(b)



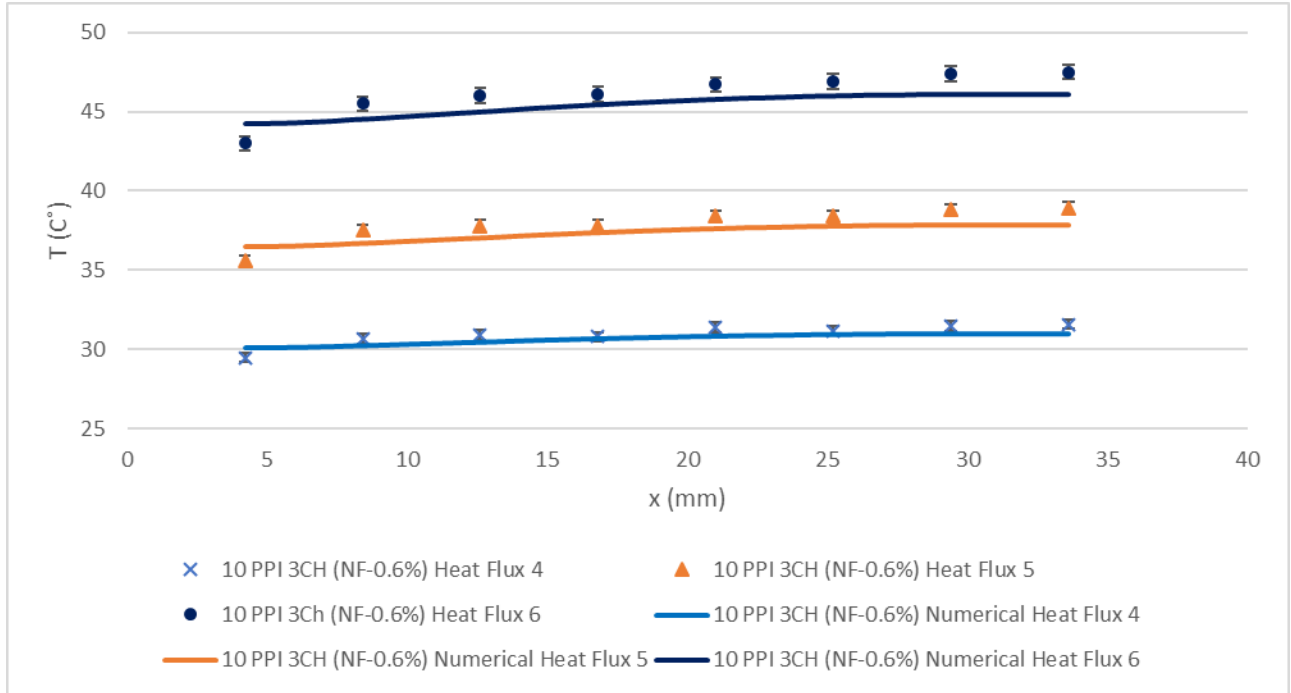
(c)

Figure 7 Varied Heat Flux Temperature Distribution at Constant Flow Rate (a) Test 1-3, (b) Test 4-6 and (c) Test 7-9

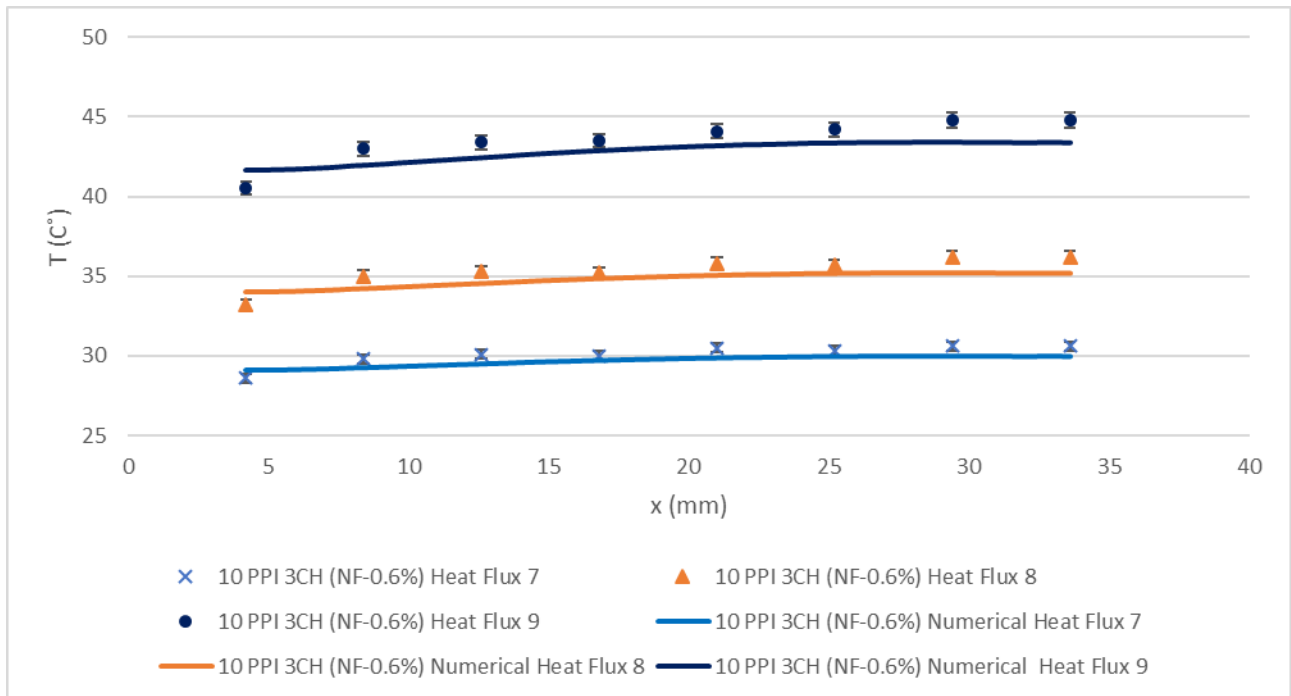
The spacing in Figure 7 (a), (b) and (c) are similar, however, (c) has the lowest temperature range. Having a lower temperature range means the thermal energy is dissipating at a more efficient rate. This occurs when the fluid velocity increases, which is caused by the increasing flow rate. The thermal boundary layers are unstable in all Tests in Figure 7. This indicates that the Reynolds number is in the transition regime. The reason that this occurs can be result of the flow collision on the flat surface on the solid fins, which causes interference with the flow path. Test 7 to 9 has the best heat transfer enhancement in this case. The next case to be discussed is 10 PPI with 0.6% alumina and three-channels, shown below in Figure 8.



(a)



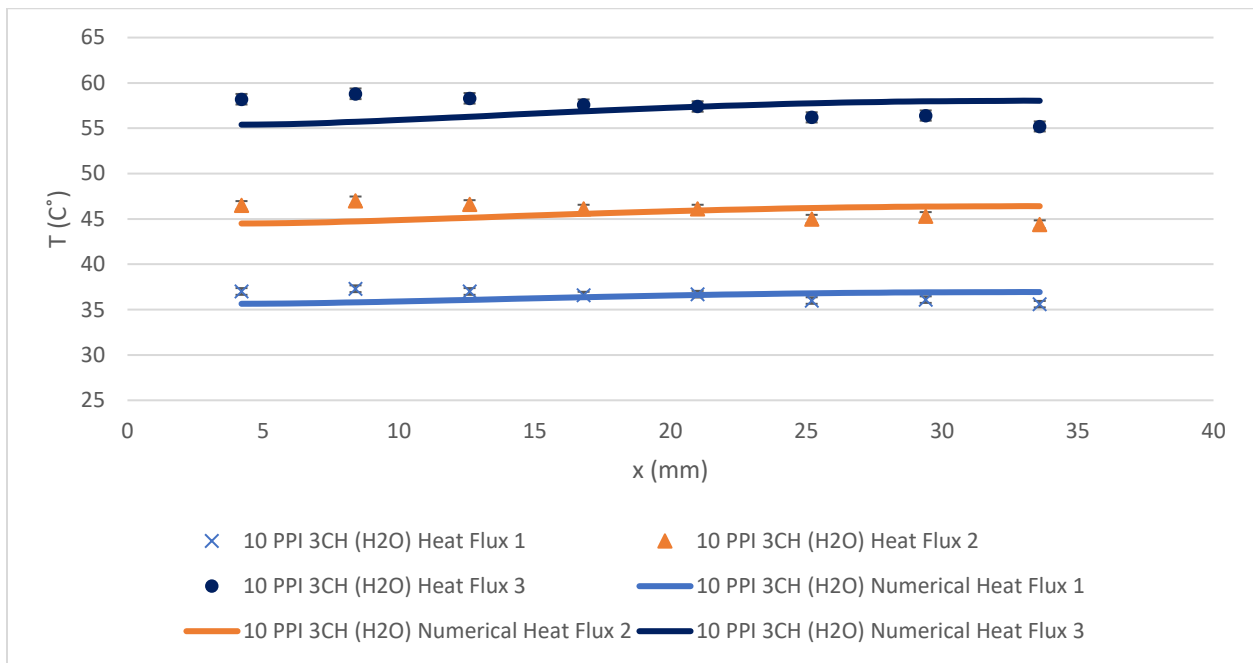
(b)



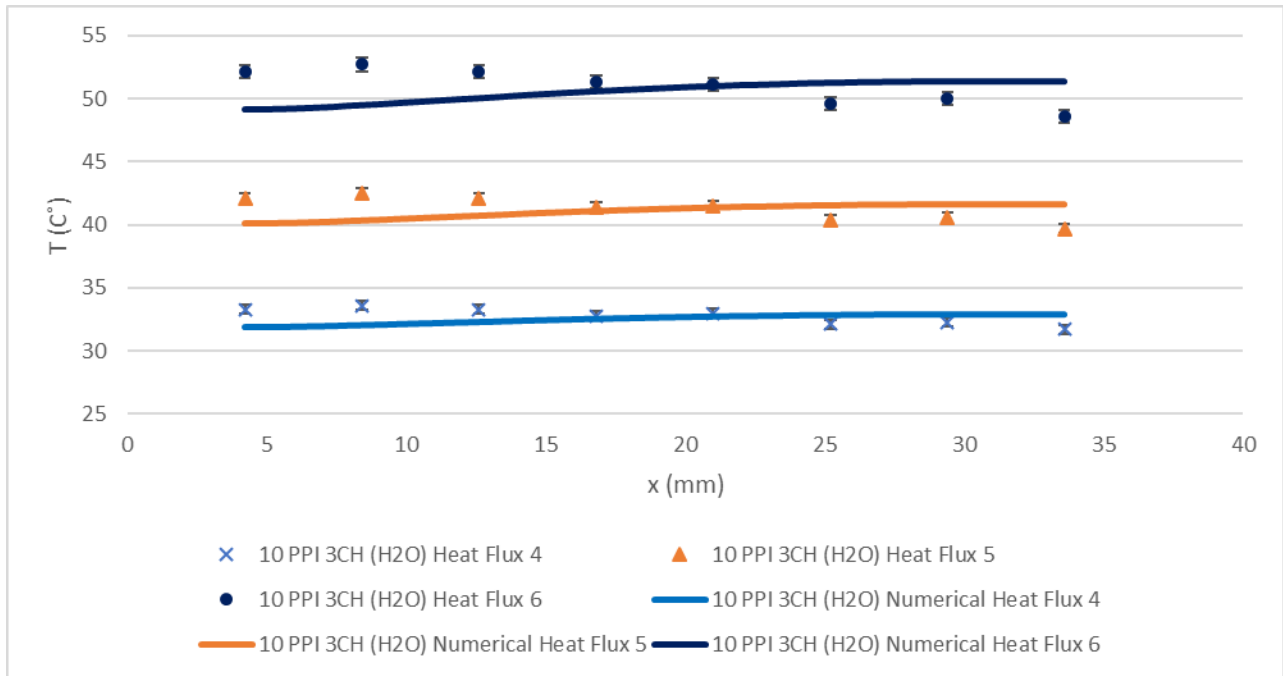
(c)

Figure 8 Varied Heat Flux Temperature Distribution at Constant Flow Rate (a) Test 1-3, (b) Test 4-6 and (c) Test 7-9

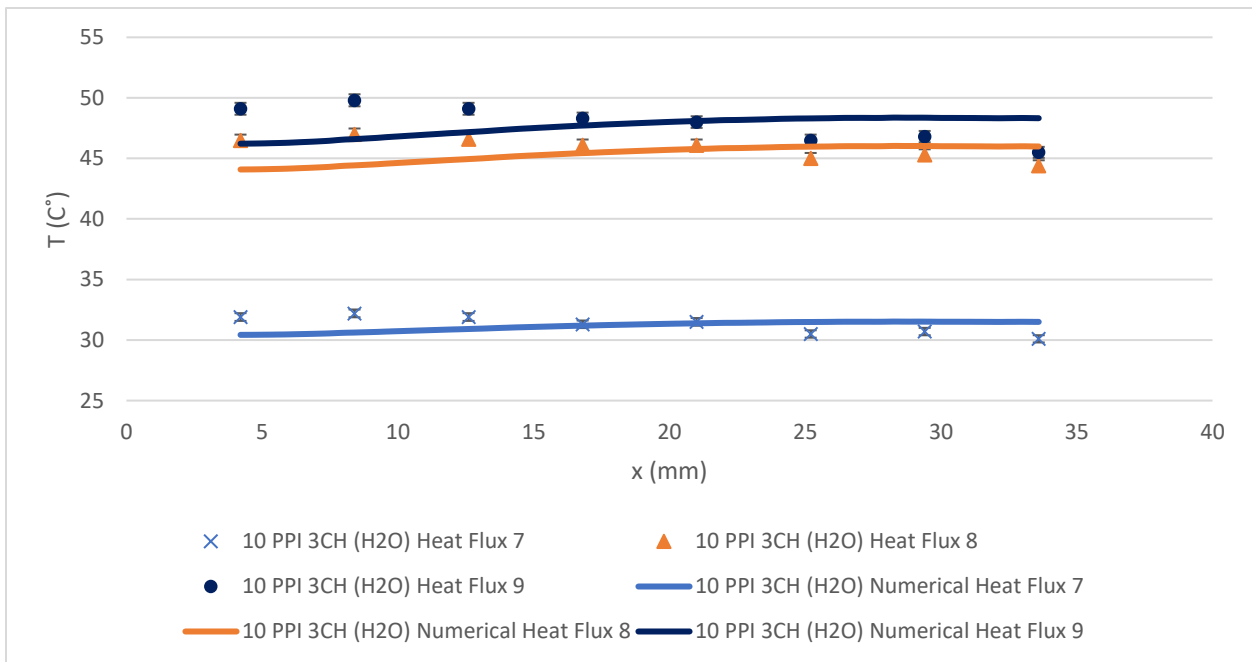
The temperature distribution in Figure 8 (a), (b) and (c) are all similar. The lowest temperature range can be seen in Figure 8 (b) and (c), however, (c) is lower. This means Figure 8 (c) has better heat transfer. The experimental and numerical data in Figure 8 (a), (b) and (c) indicates a stable thermal boundary layer. This means that the Reynolds number is in the laminar region. The reason being that there is no interference with the flow path into the three-channels test block. Test 7 to 9 has the best heat transfer enhancement in this case. The next case that is discussed is the 10 PPI with distilled water and three-channels, which is shown below in Figure 9.



(a)



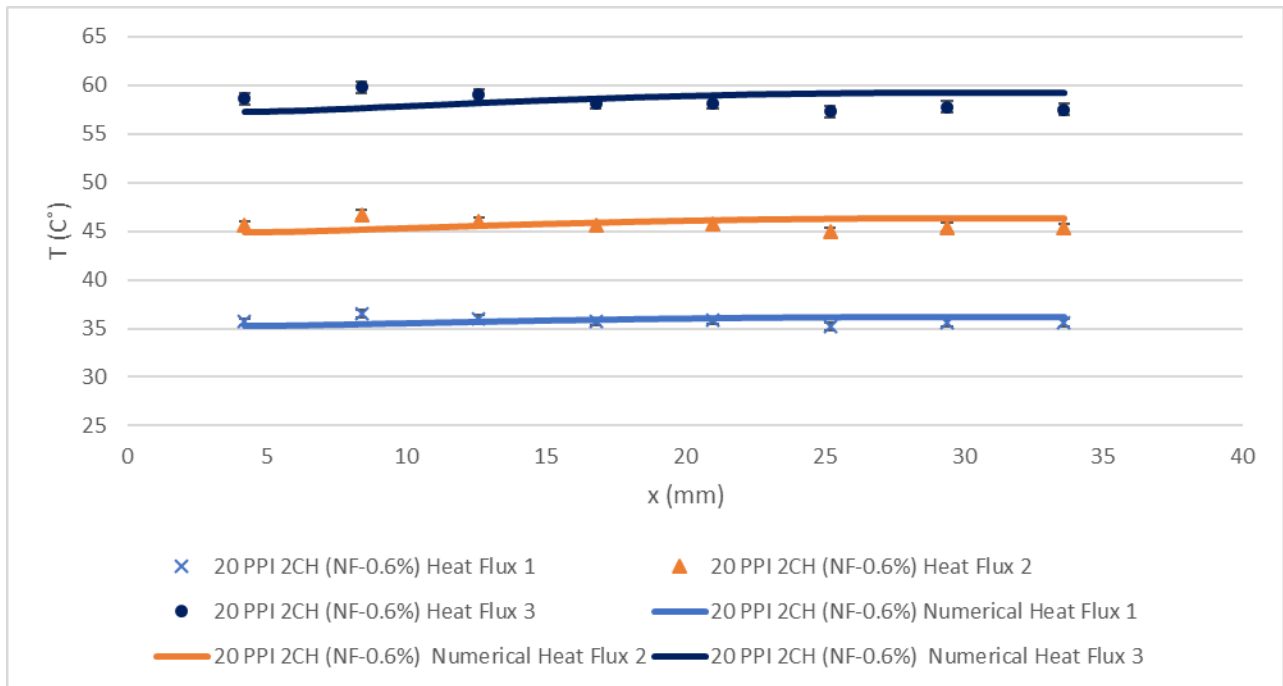
(b)



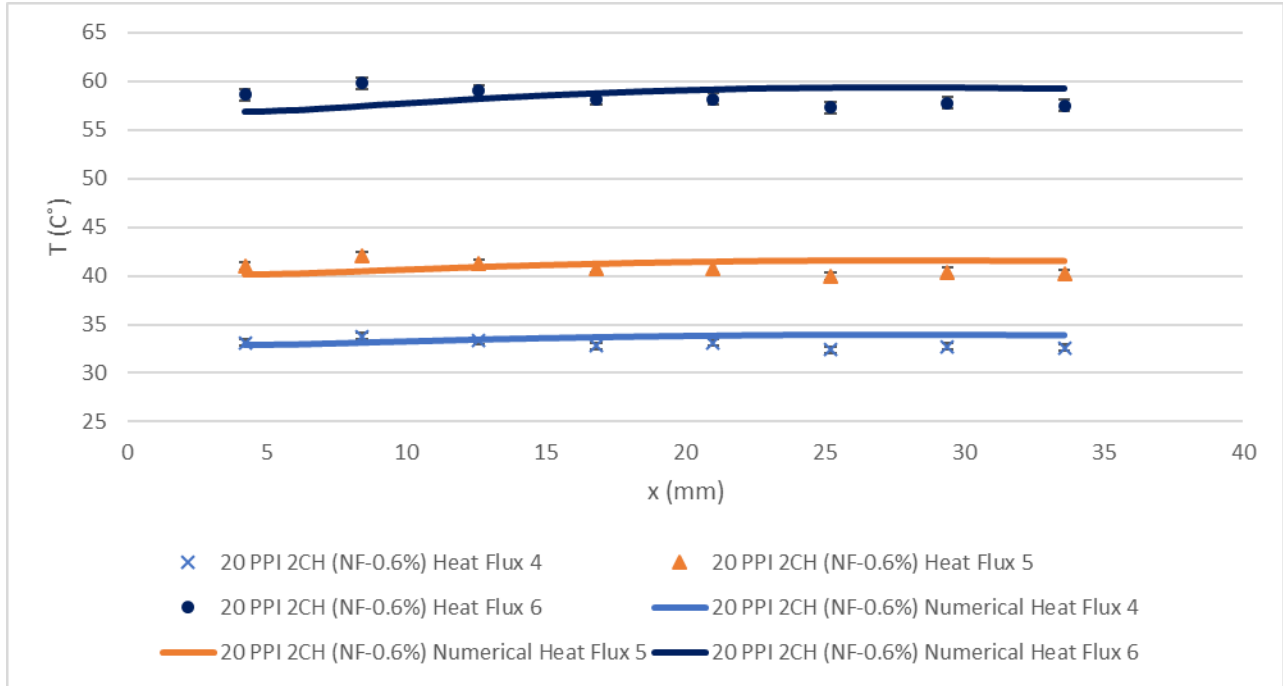
(c)

Figure 9 Varied Heat Flux Temperature Distribution at Constant Flow Rate (a) Test 1-3, (b) Test 4-6 and (c) Test 7-9

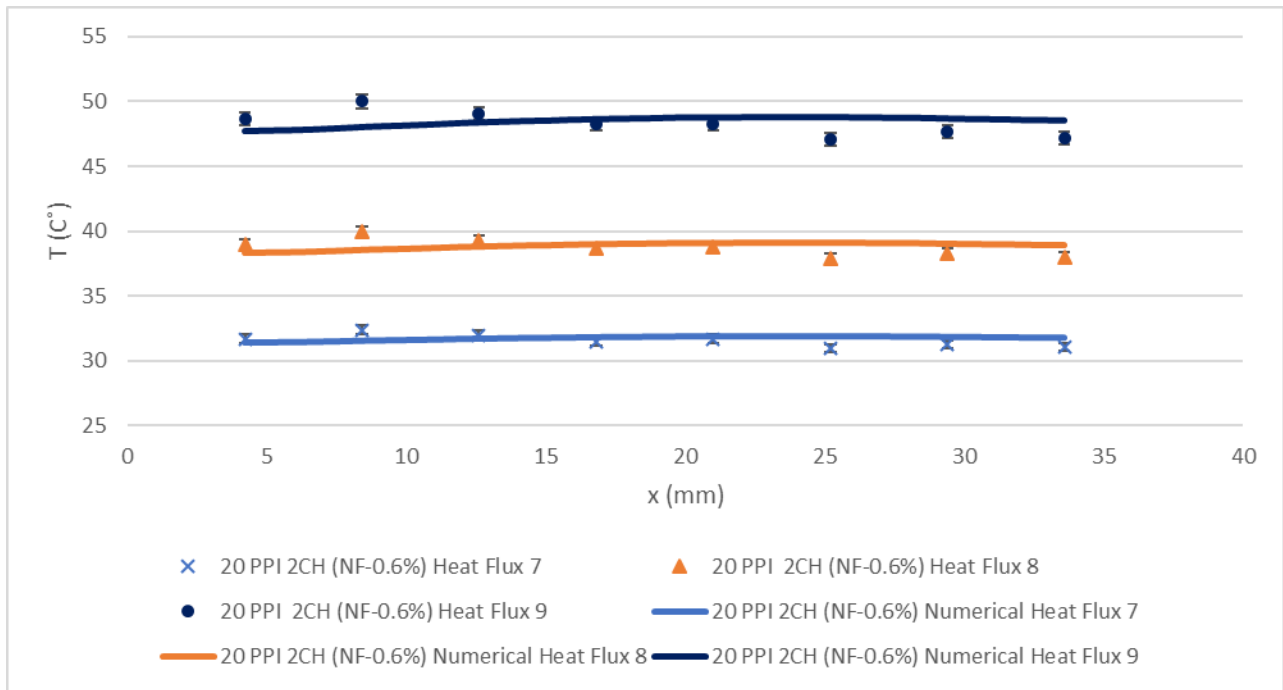
As shown above, Figure 9 (a) and (b), have similar spacing, however, (c) has the lower temperature range. This indicates a heat transfer enhancement. When analyzing Figure 9 (c) the spacing between the heat fluxes do not have uniform spacing, but the order in which the heat fluxes appear are expected. The results from Figure 9 (c) is a result of experimental deviation. The numerical data deviates as well because of the use of the experimental data. In Figure 9, the data points do not represent a uniform thermal boundary layer. A non-uniform thermal boundary layer occurs in transitional Reynolds number region. The viscosity of distilled water is less than nanofluid with 0.6% alumina. Having a lower viscosity results in a larger Reynolds number, which in this case had a value in the transitional region. Since Test 7 to 9 has experimental deviation, Test 4 to 6 performs best in this case. Shown below in Figure 10 is the 20 PPI with nanofluid and two-channels case.



(a)



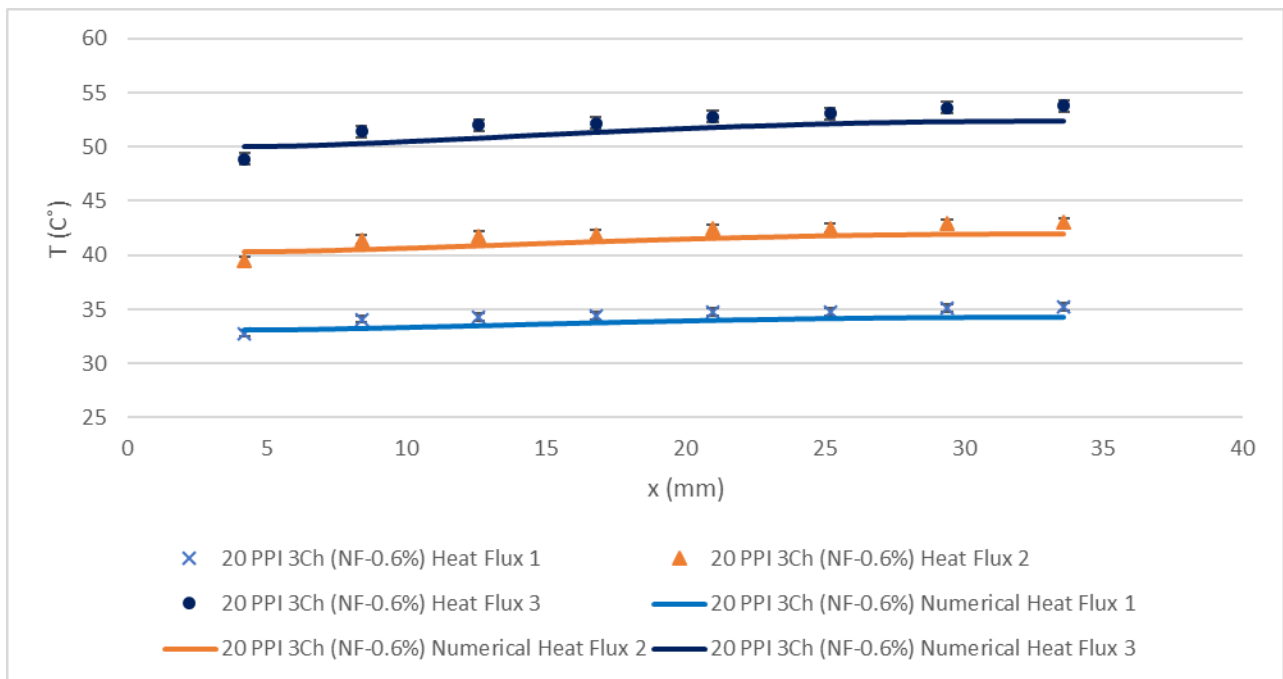
(b)



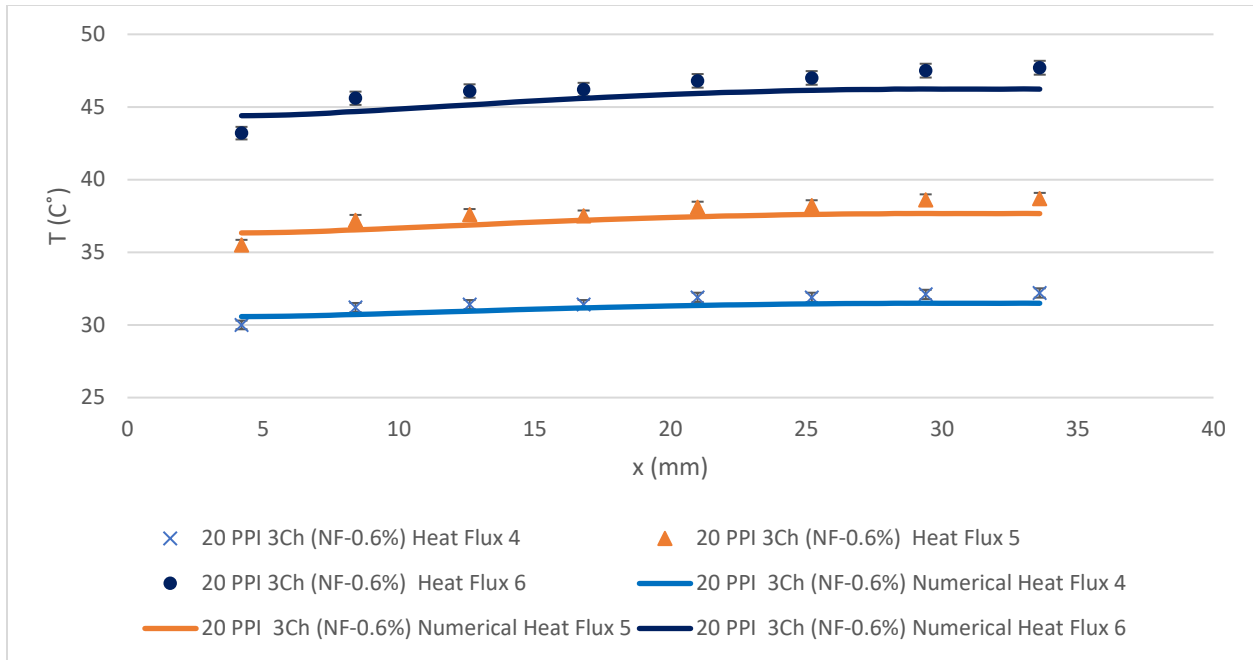
(c)

Figure 10 Varied Heat Flux Temperature Distribution at Constant Flow Rate (a) Test 1-3, (b) Test 4-6 and (c) Test 7-9

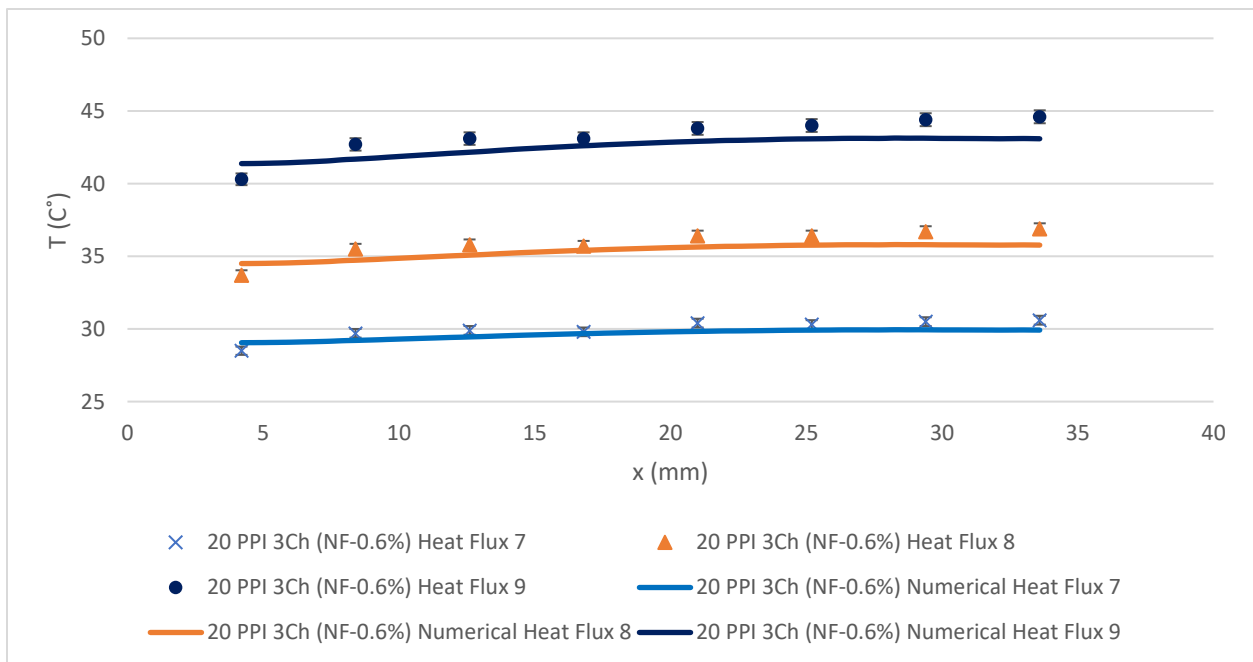
The spacing between each Test in Figure 10 (c) are evenly spaced and has the lowest temperature range. As the heat flux is constantly heating up the test block, the increase in flow rate removes the heat more efficient and effectively than Figure 10 (a) and (b) Tests. Thus, a higher rate of heat transfer occurs, making Test 7 to 9 the best in this case. It is important to note that the thermal boundary layer is unstable in Figure 10, which is shown in the experimental data points. An unstable thermal boundary layer means the flow is not laminar but in the transitional region of the Reynolds number. The occurrence of this is from the flow path being interrupted when the fluid enters from the inlet and collides with flat surface of the center fin, which is present in the two-channels test block. The case that is discussed next is for 20 PPI with nanofluid and three-channels, this is seen in Figure 11 below.



(a)



(b)

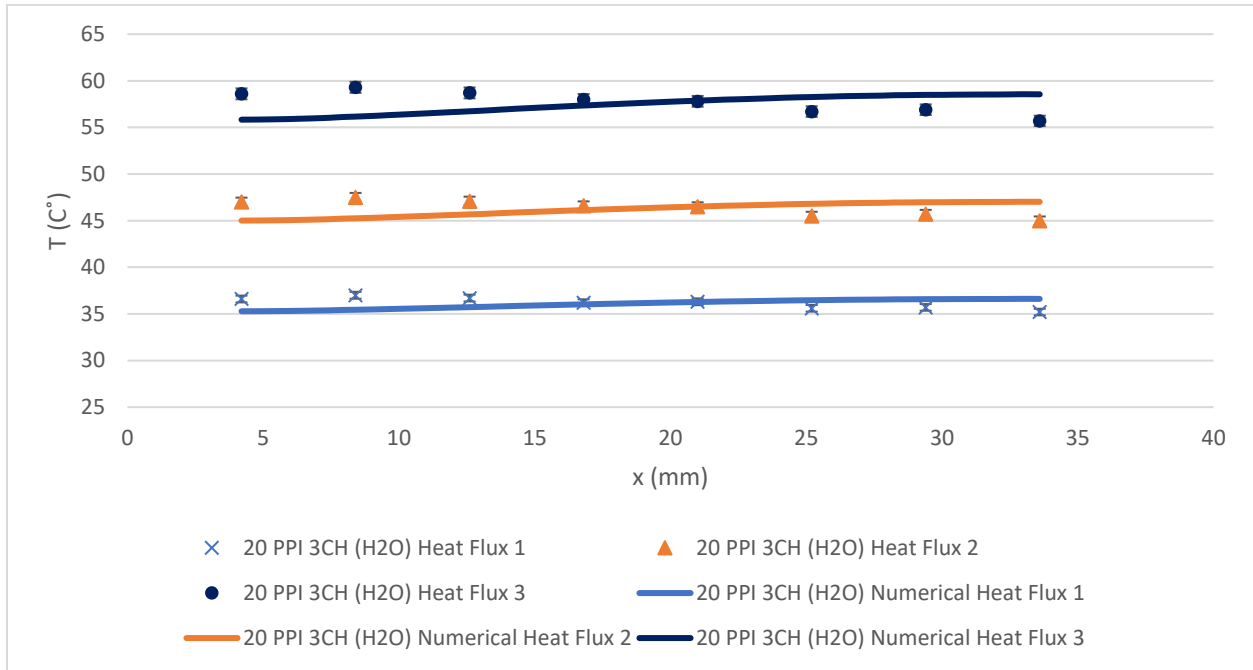


(c)

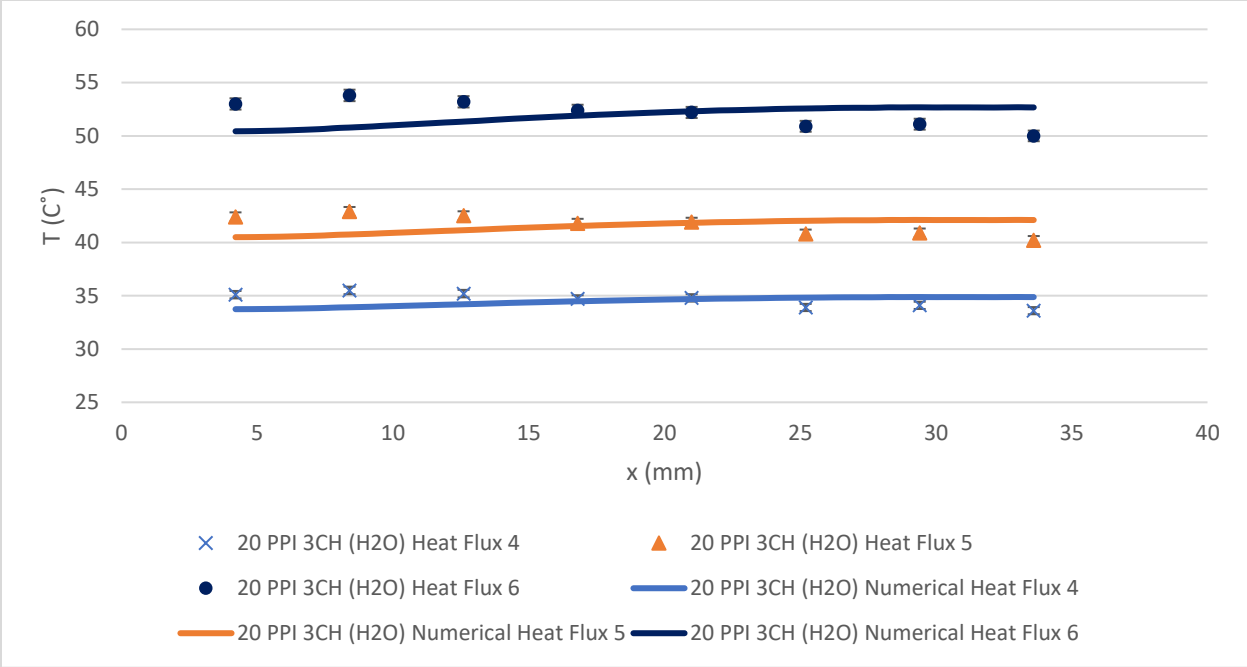
Figure 11 Varied Heat Flux Temperature Distribution at Constant Flow Rate (a) Test 1-3, (b) Test 4-6 and (c) Test 7-9

In Figure 11 (c), it has the lowest temperature range when compared to (a) and (b). A lower temperature range is important because it suggests that the removal of thermal energy is occurring

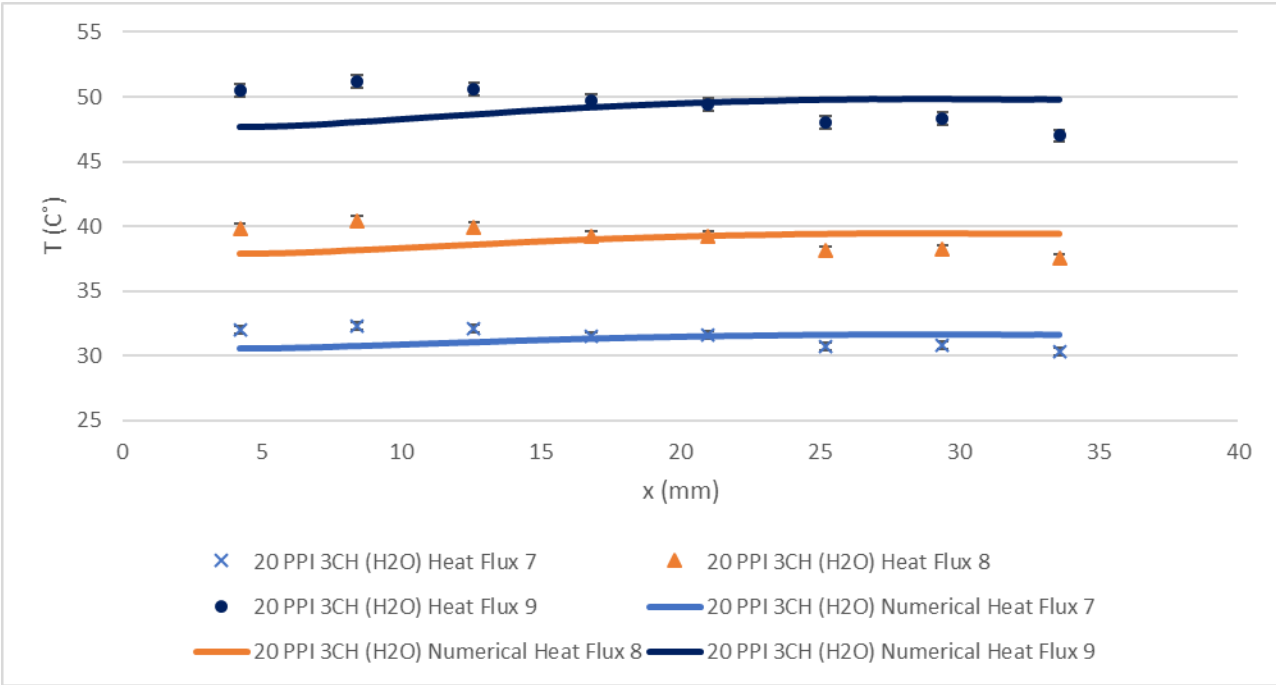
at a higher rate. For Test 7 to 9 there is even spacing. Even spacing represents the uniform increase in temperature with a constant heat flux. In Figure 11 (a), (b) and (c), the experimental data points illustrate a uniform thermal boundary layer. What this means is the Reynolds number is in the laminar region. In this case, Test 7 to 9 have the best results. The last case to be discussed is 20 PPI with distilled water and three-channels.



(a)



(b)



(c)

Figure 12 Varied Heat Flux Temperature Distribution at Constant Flow Rate (a) Test 1-3, (b) Test 4-6 and (c) Test 7-9

Figure 12 (a), (b) and (c) have uniform spacing. The figure that has the lowest temperature range is (c), which indicates the tests with the best heat transfer enhancement. The curves of the experimental data points do not show a steady thermal boundary layer. This means Figure 12 (a), (b) and (c) are in the transitional regime of the Reynolds number. The occurrence of this is caused from the low viscosity of distilled water, when compared to nanofluid. A low viscosity proportionally increases the Reynolds number. In this case increasing the Reynolds number into the transitional regime. In this case, Test 7 to 9 gives the optimal results. The cases that performed the best is 10 and 20 PPI with nanofluid and three channels. The reason being that they have a stable thermal boundary layer in the laminar regime. The two cases are used to compare and analyze the other results.

4.2 The Effects of Channels

The best cases found in the previous section, 10 and 20 PPI with nanofluid and three-channels, will be compared with 10 and 20 PPI with nanofluid and two-channels, respectively. As well only Test 7 to 9 for each case will be compared. The reason being is that they are the best performing nominal heat fluxes for each case stated above. The first comparison is the 10 PPI with nanofluid versus three and two channels, which is shown below in Figure 13. It is important to note that the thermal boundary layer is unstable for the two-channels cases discussed below (Figure 13 and Figure 14). Thus, the two-channels cases are in the transitional regime. While in the three-channels cases, the thermal boundary layer is stable and in the laminar regime, which is shown in Figure 13 and Figure 14. This is an important relationship because, it demonstrates that the number of channels effects the thermal boundary layer.

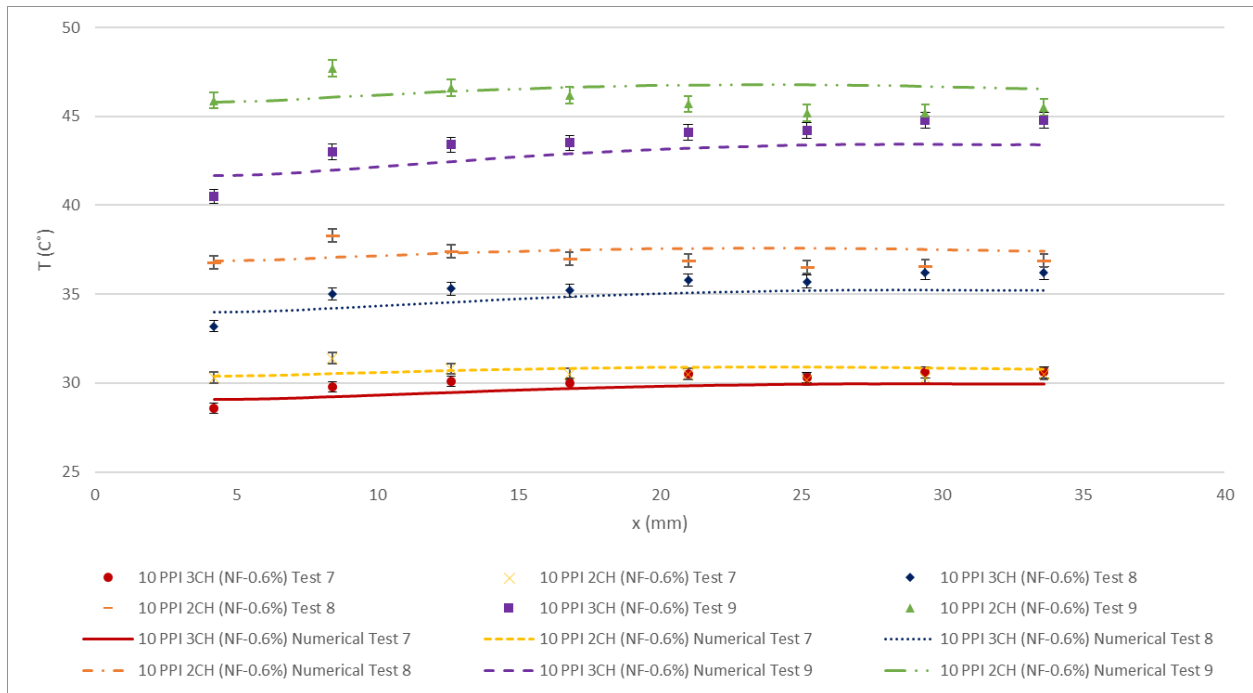


Figure 13 Two-Channels versus Three-Channels Temperature Distribution for Test 7, Test 8 and Test 9

By analyzing Figure 13, it clearly shows that three-channels gives a lower temperature distribution. Therefore, heat transfer enhancement is improved with the three-channels cases. The improvement in the temperature distribution is caused by the increase in the fluid velocity. The fluid velocity is directly related to the cross-sectional area, which is related to the number of channels. What this means is that more channels equal an increase in velocity. This leads to the three-channels case having the best improvement in heat transfer. The temperature is increasing for each Test, 7, 8 and 9, with the increasing value of the nominal heat fluxes of 60,000, 84,000 and 111,000 W/m², respectively. It is behaving as expected with no abnormalities. The next case to be discussed is the 20 PPI with nanofluid versus three and two-channels, which can be seen in Figure 14.

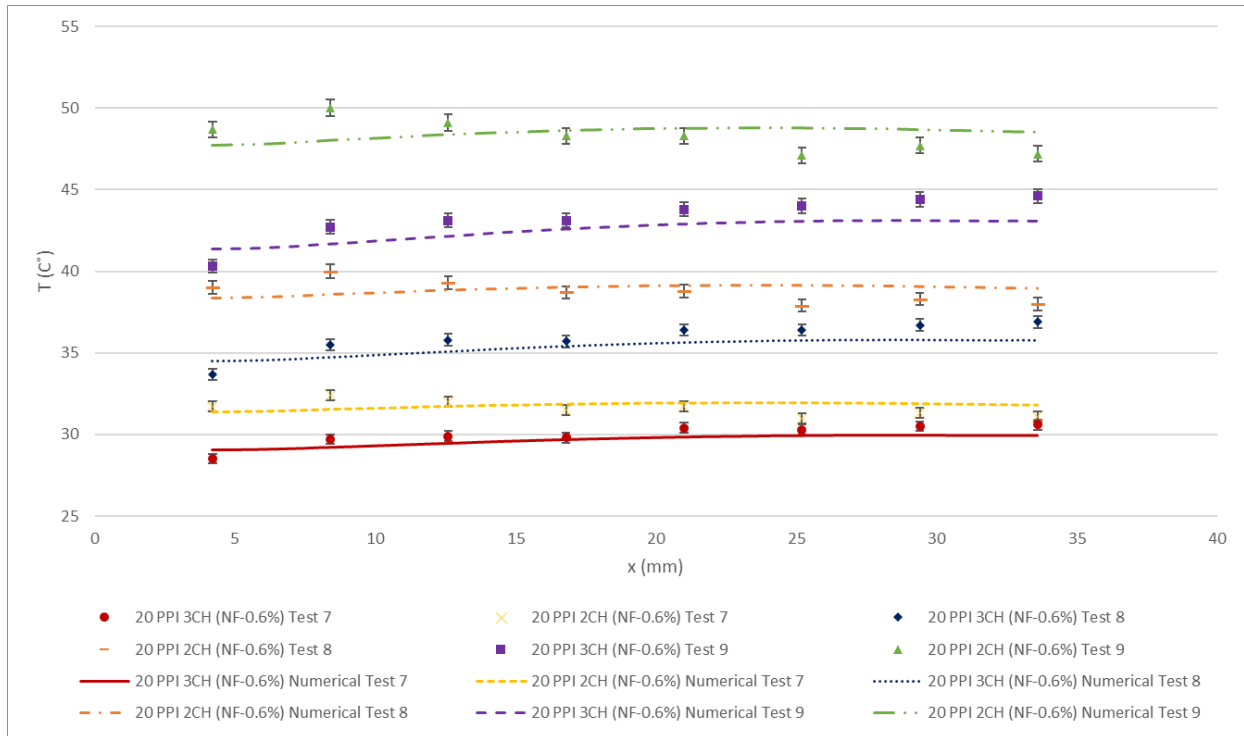


Figure 14 Two-Channels versus Three-Channels Temperature Distribution for Test 7, Test 8 and Test 9

In Figure 14, the three-channels Tests, 7, 8 and 9, have the lowest temperature distribution when compared with the two-channels results. This means that the three-channels case has a larger improvement in heat transfer enhancement than two-channels. This result is caused by the increases in velocity, and having a larger velocity means more heat can be removed from the test block. The increasing of the velocity occurs when there is an increase in the cross-sectional area, via the addition of a channel. Thus, three-channels lead to the best heat transfer enhancement. The increasing values of the nominal heat fluxes for Test 7,8 and 9 are proportionally increasing the temperature. This occurs for both cases. The values of the nominal heat flux for Test 7,8 and 9 are the following: 54,000, 84,000 and 111,000 W/m^2 , respectively. The behavior of the nominal heat flux and temperature increase is as expected.

4.3 The Effects of Concentration

The two best cases in section 3.1 (The Effects of Heat Flux), are the 10 and 20 PPI with nanofluid and three-channels. They are compared with their respective 10 and 20 PPI with distilled water

and three-channels cases. The Tests that are selected for the 10 PPI cases are Test 4, 5, 6, 7, 8, and 9. A larger range of tests are selected because of the experimental deviation presented in the 10 PPI with distilled water and three-channels case. The Tests that are selected for the 20 PPI case are Test 7, 8 and 9. The 10 PPI cases will be shown first, which is seen in Figure 15 and Figure 16. It is important to note that the thermal boundary for the distilled water cases are not stable, which can be seen in Figure 16 and Figure 17. The reason being is distilled water has a lower viscosity than the nanofluid used in the experiment. The viscosity is directly proportional to the Reynolds number, which resulted in a value in the transitional regime. While the addition of nanofluid gives a stable thermal boundary layer, which is in the laminar regime. This can be seen in Figure 16 and Figure 17 below. This is an important relationship because, this indicates that by adding nanofluid to the three-channels cases a stable thermal boundary layer is achieved.

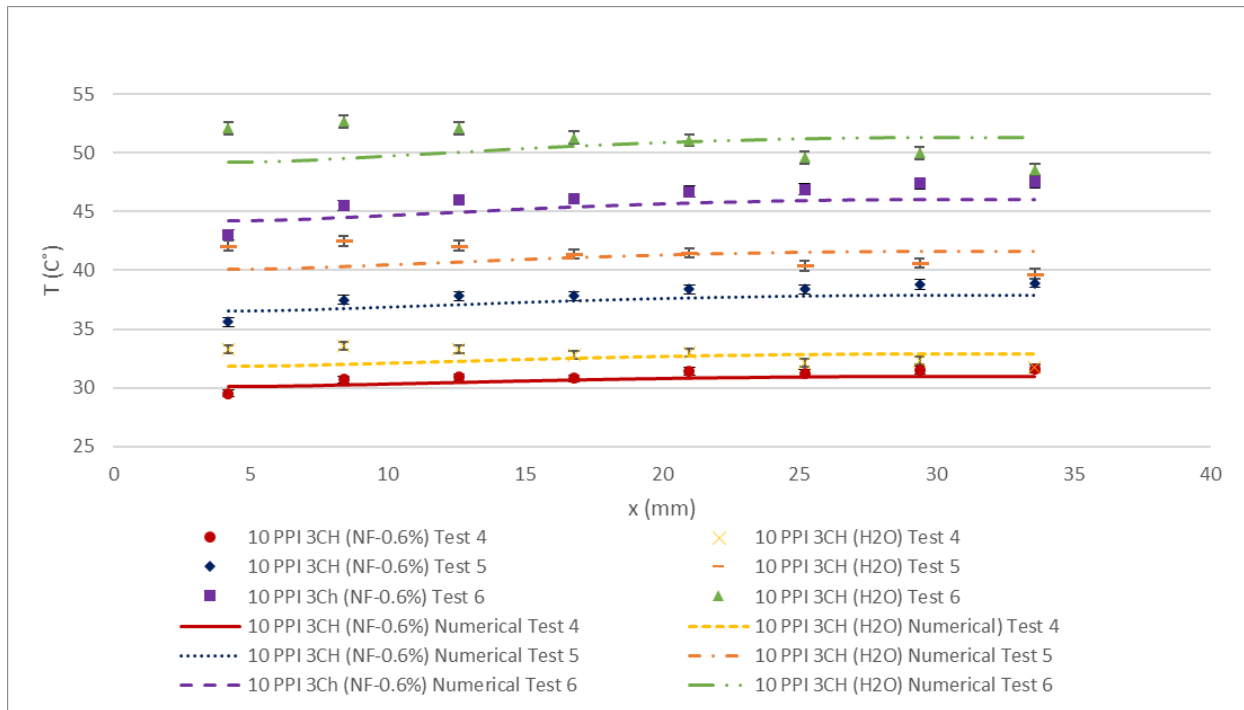


Figure 15 Nanofluid versus Distilled Water with Temperature Distribution for Test 5 and Test 6

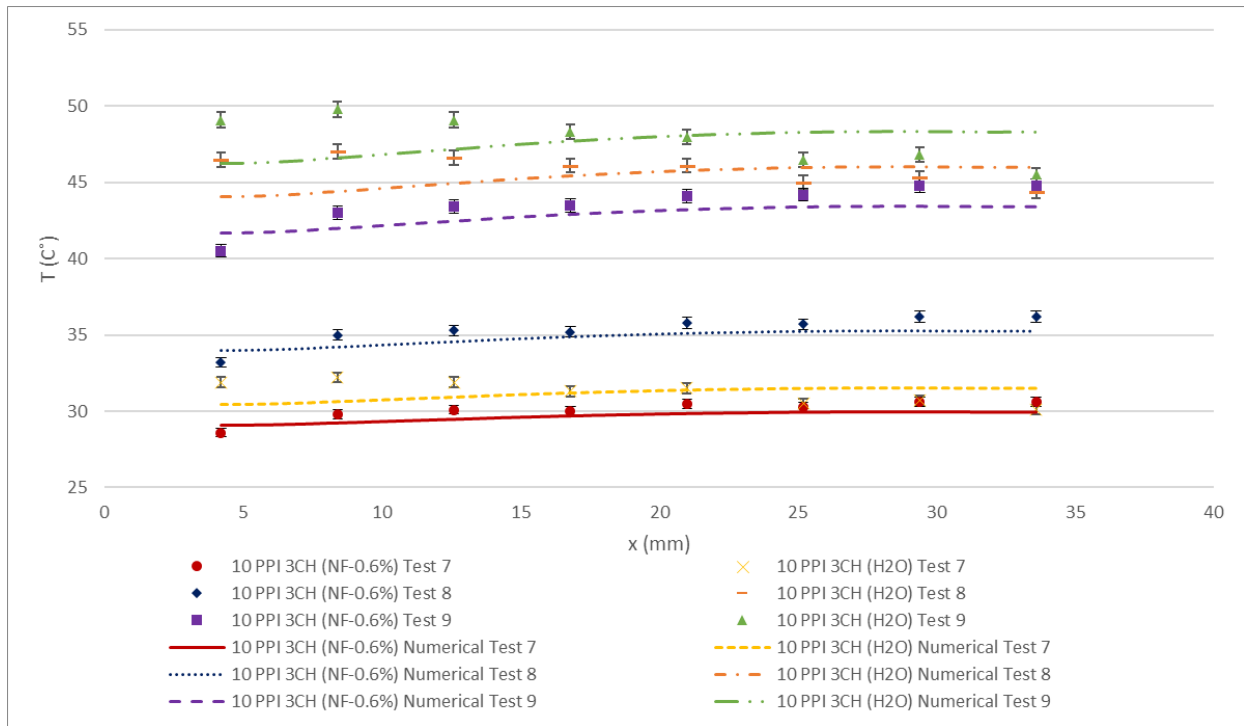


Figure 16 Nanofluid versus Distilled Water with Temperature Distribution for Test 7, Test 8 and Test 9

It can be seen in Figure 15 and Figure 16 that the addition of nanofluid gives a lower temperature distribution than with just distilled water. This means that the addition of the nanofluid provides a heat transfer enhancement. The addition of the nanoparticles allows more thermal energy to be absorbed and transported through the outlet of the test block. As well as the increase in the thermal conductivity. The next case to be discussed is the 20 PPI with nanofluid versus distilled water and three-channels, shown below in Figure 17.

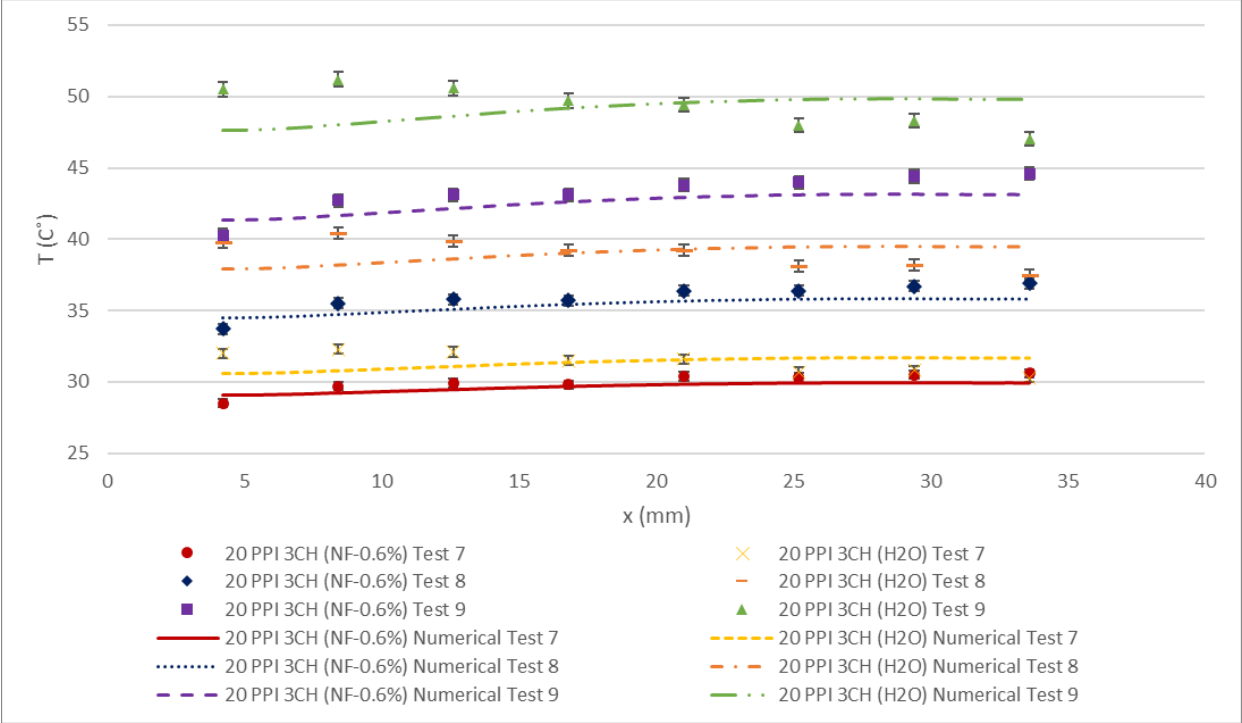


Figure 17 Nanofluid versus Distilled Water with Temperature Distribution for Test 7, Test 8 and Test 9

In Figure 17, the nanofluid has a lower temperature distribution than distilled water. This means at the same parameters as distilled water (flow rate, nominal heat flux, three-channels, and permeability), nanofluid is able to remove thermal energy at a more efficient rate. The nanoparticles (alumina) added to the nanofluid allows for more thermal energy to be absorbed, thus increasing the efficiency of heat transfer. This is the effect of the increased thermal conductivity.

4.4 The Effects of Flow Rate

The cases that are analyzed are the 10 and 20 PPI with nanofluid and three-channels. The particular Tests that are compared are Test 1, 4 and 7, which are shown below in Figure 18. It is important to note that the thermal boundary layer for both cases are stable, which is shown below in Figure 18. A stable thermal boundary layer means that it is in the laminar regime.

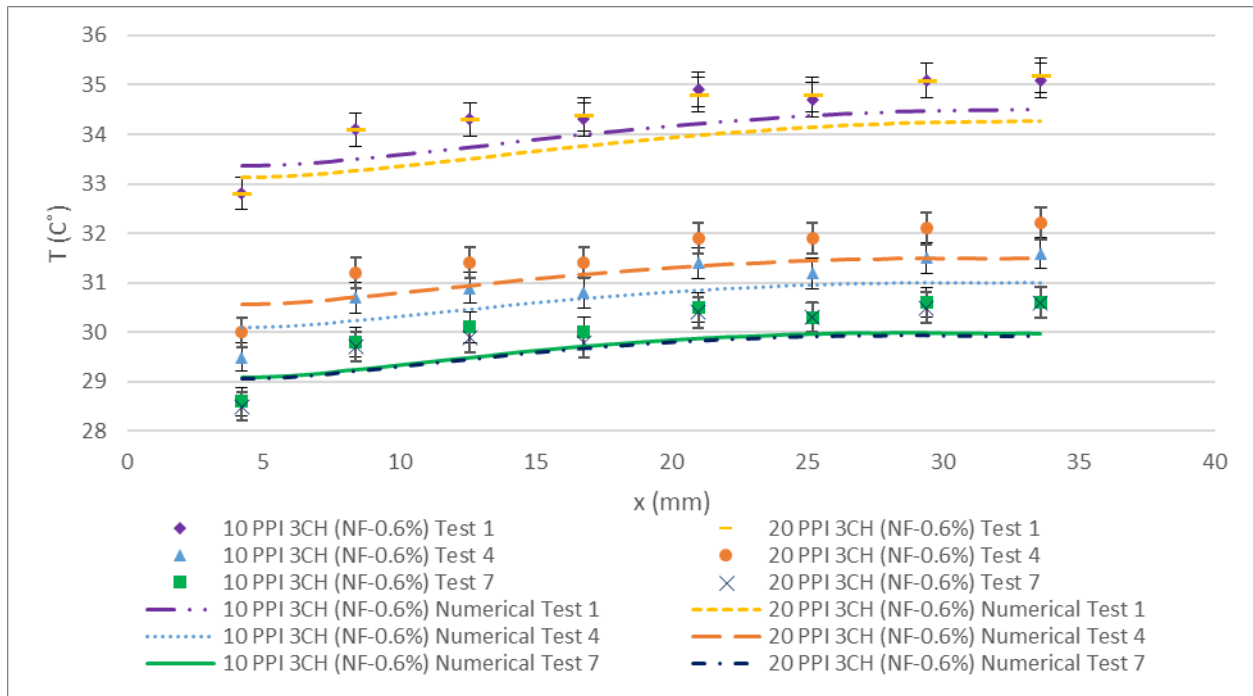


Figure 18 The Effects of Flow Rates on the Temperature Distribution for Test 1, Test 4 and Test 7

The flow rates associated with Test 1, 4 and 7 in Figure 18 are the following: 0.1, 0.2 and 0.3 USGPM. The temperature distribution for Test 7 is lower than Test 1 and 4, which coincides with the other results analyzed in previous sections. A lower temperature distribution means there is better heat transfer. Also, in Test 7 the flow rate has negligible effect between the two cases. Meaning, the heat transfer enhancement is similar for both cases. The pressure drop for 20 PPI is higher than 10 PPI, because the packing of the pores are tighter, therefore more resistance to flow. Higher pressure drop equals a reduction in heat transfer enhancement. In general, for Test 1 and 4, the temperature difference between the two cases is approximately one degree, which is due to the higher pressure drop in the 20 PPI case. The nominal heat flux used is $55,500 \text{ W/m}^2$. The higher flow rates are able to dissipate more of the thermal energy, which is expected. Higher flow rate means more volume mass can be carried out of the test block at a more efficient rate.

4.5 The Effects of Permeability

The effects of permeability will be discussed. The 10 and 20 PPI with nanofluid and three-channels cases will be analyzed. The Tests used are 7 to 9, which is shown below in Figure 19. It is important to note that the thermal boundary layer is stable for the cases shown below, which is shown below in Figure 19.

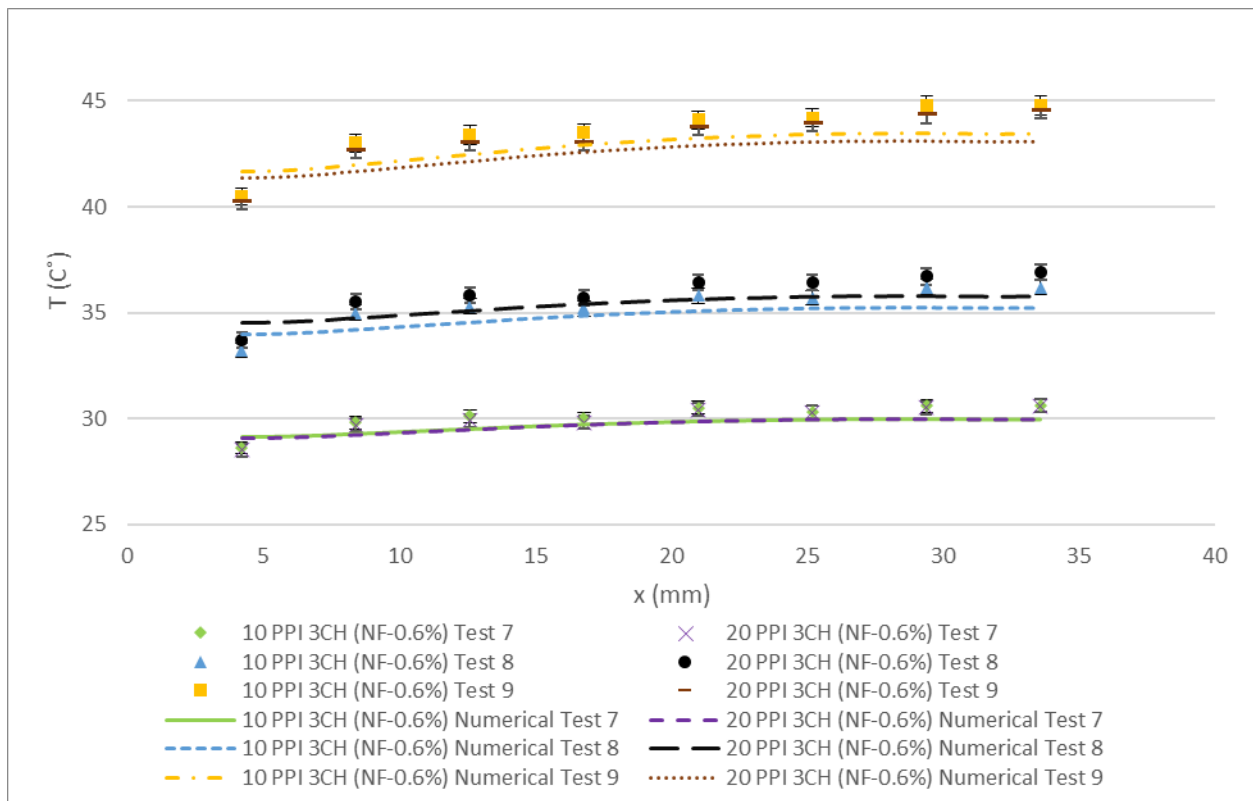


Figure 19 The Effects of Permeability on Temperature Distribution for Test 7 to 9

Analyzing Figure 19, the permeability does not affect the temperature distribution, therefore, both cases have negligible difference for heat transfer enhancement. The 20 PPI pores are packed tighter, which means there is more resistance to the flow. Thus, the flow rate (0.1 USPGM) is not high enough to break the surface tension between each pore. Resulting in the same heat transfer enhancement as the 10 PPI case.

4.6 The Rate of Removal of Thermal Energy

The average Nusselt number is used to determine which case(s) has the optimal rate of removal of thermal energy. All the results are shown below in Figure 20.

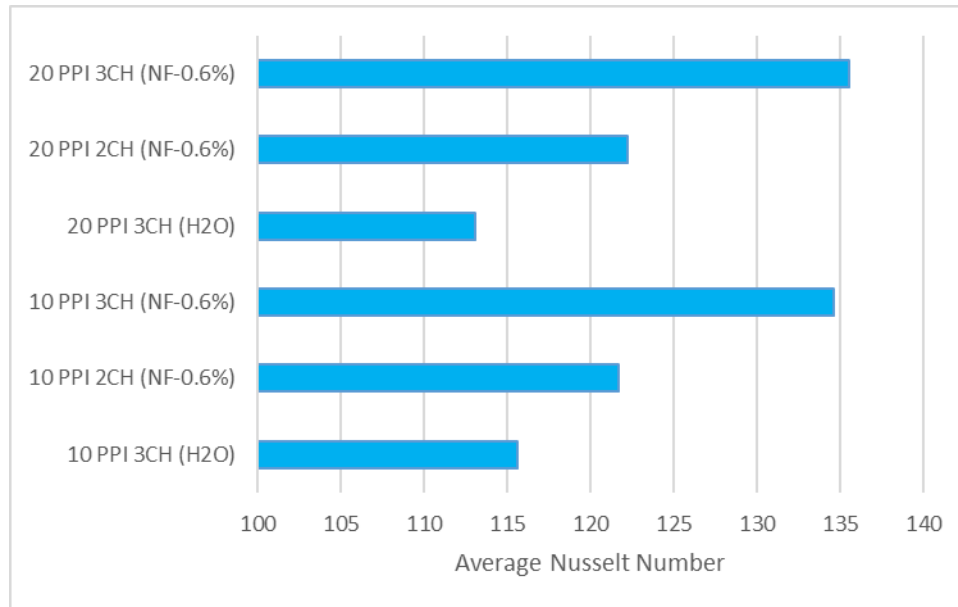


Figure 20 Average Nusselt Number for the Six Cases

When comparing the distilled water and nanofluid in Figure 20, there is a significant difference in the average Nusselt number. This means that the nanofluid has better heat transfer enhancement, which is expected. In Section 3.3 (The Effects of Concentration), it was found that the addition of the nanofluid increased the thermal conductivity of the fluid, thus allowing for more thermal energy to be absorbed. Another observation is that the three-channels cases have the largest average Nusselt number, when compared to the two-channels. The larger Nusselt number is a result of the increased fluid velocity, which is dependent on the cross-sectional area. More channels equal a higher velocity, in this case three. This is mentioned in Section 3.2(The Effects of Channels). The average Nusselt number for the 10 and 20 PPI with nanofluid and three-channels are similar: 134.6 and 135.5, respectively. From Section 3.6 (The Effects of Permeability), the heat transfer enhancement factor between 10 and 20 PPI are negligible. The permeabilities of 10 and 20 PPI are similar, they are both to the factor of 10^{-7} . The case that had

the maximum Nusselt number is 20 PPI with nanofluid and three-channels. The value is 135.5. The average Nusselt number results re-enforce the findings found in the previous sections.

4.7 The Effects of Pressure Loss on Pumping Power

The pressure loss is analyzed and compared for all six of the cases. Having a lower pressure loss is important, because it indicates the amount of pumping power required for the system. Shown below in Figure 21 are the pressure losses. It is important to note that the pressure loss values are numerically derived.

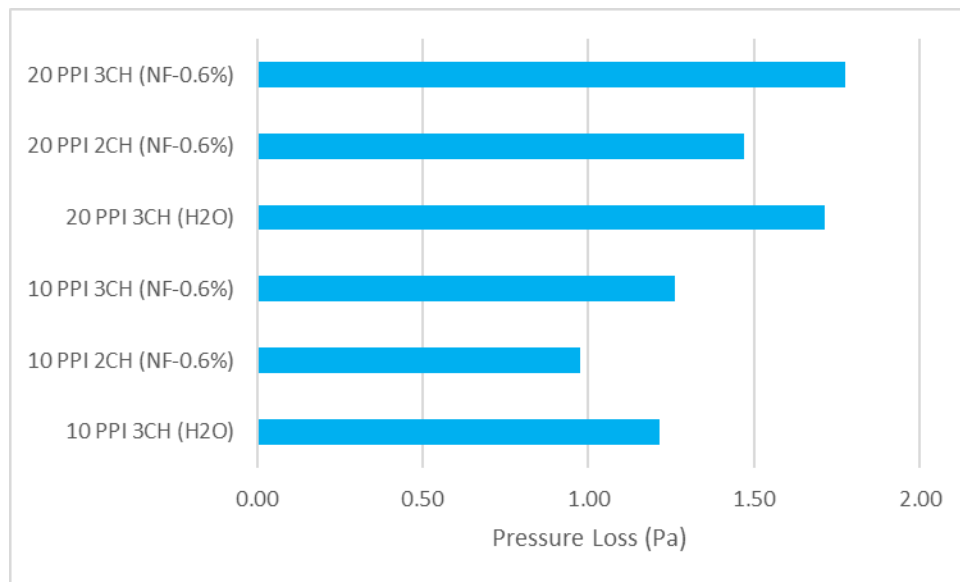


Figure 21 Pressure Lose for the Six Cases

When looking at the permeability, 10 and 20 PPI, it can be seen in Figure 21 that all the 10 PPI cases have a lower pressure loss. In 20 PPI, there is a higher density of pores, therefore, a lower permeability when compared to 10 PPI. This means that there is more flow resistance. The concentrations, nanofluid with 0.6% alumina and distilled water, have a minor effect on the pressure loss. The addition of the nanofluid increases the pressure loss because of the increase in viscosity. The number of channels greatly affect the pressure loss. The two-channels cases have

a smaller pressure loss than three-channels because there is less interference with the walls. The case that has the smallest pressure drop is 10 PPI with nanofluid and two-channels. The value is 0.97 PPI. It is believed this case is optimal because it requires the least amount of pumping power. This is important because less pumping power reduces operational cost.

5 Conclusion and Future Work

This section will summarize the important findings in the results and discussion section. As well as discuss future work.

5.1 Conclusion

The author has successfully analyzed the six numerical and experimental cases, which are 10 and 20 PPI with nanofluid or distilled water, and three-channels or two-channels. The nanofluid that is used is 0.6% alumina. It is important to note that the studies modeled an intel core i7 processor. The main conclusions that are found for the experimental and numerical study are the following:

- The maximum average Nusselt number that is found for the 20 PPI with nanofluid and three-channels case, which is important for rate of removal of thermal energy
- The case that has the smallest pressure loss is 10 PPI with nanofluid and two-channels,
- The temperature distribution gives favorable results for the 10 and 20 PPI with nanofluid and three-channels
- The flow rate that gave the best temperature distribution is 0.3 USGPM
- The permeability has negligible effect on the temperature distribution, because the permeability of 10 and 20 PPI are both 10^{-7}
- The three-channels cases have the lowest temperature distribution
- It is important to note that if having a lower pumping power is desired then the 10 PPI with nanofluid and two-channels should be used, and if having a lower temperature distribution is desired the 20 PPI with nanofluid and three-channels should be used
- The thermal boundary layer is stable for the 10 and 20 PPI with nanofluid and three-channels cases
- The average relative error between experimental and numerical cases is 3.57%

5.2 Future Work

The future work should continue by investigating into the flow rate, wavy channels and hybrid nanofluid. The flow rate should be increased to see if there is a maximum point of improvement. The wavy channels are an interesting design feature because the working fluid will have more time for the heat transfer effect. The hybrid nanofluid will be added to a modified experimental apparatus that is used in this paper. The purpose is to investigate the heat transfer enhancement potential of the hybrid nanofluid.

References

- [1] C. J. Ho, W. K. Liu, Y. S. Chang and C. C. Lin, "Natural convection heat transfer of alumina-water nanofluid in vertical square enclosures: An experimental study," *International Journal of Thermal Sciences*, no. 49, pp. 1345-1353, 2010.
- [2] C. J. Ho, L. C. Wei and Z. W. Li, "An experimental investigation of forced convective cooling performance of a microchannel heat sink with Al₂O₃/water nanofluid," *Applied Thermal Engineering*, no. 30, pp. 96-103, 2010.
- [3] C. J. Ho and W. C. Chen, "An experimental study on thermal performance of Al₂O₃/water nanofluid in a minichannel heat sink," *Applied Thermal Engineering*, no. 50, pp. 516-522, 2013.
- [4] E. Pourfarzad, K. Ghadiri, A. Behrangzade and M. Ashjaee, "Experimental investigation of heat transfer and pressure drop of alumina–water nano-fluid in a porous miniature heat sink," *Experimental Heat Transfer*, vol. 31, no. 6, pp. 495-512, 2018.
- [5] N. Bouguerra, S. Poncet and S. Elkoun, "Dispersion regimes in alumina/water-based nanofluids: Simultaneous measurements of thermal conductivity and dynamic viscosity," *International Communications in Heat and Mass Transfer*, pp. 51-55, 2018.
- [6] Y. Wang, K. Deng, J. Wu , G. Su and S. Qiu , "The characteristics and correlation of nanofluid flow boiling critical heat flux," *International Journal of Heat and Mass Transfer*, pp. 212-221, 2018.
- [7] A. K. Tiwari, P. Ghosh and J. Sarkar, "Particle concentration levels of various nanofluids in plate heat exchanger for best performance," *International Journal of Heat and Mass Transfer* , pp. 1110-1118, 2015.
- [8] M. A. Nazari, R. Ghasempour , M. H. Ahmadi, G. Heydarian and M. B. Shafii, "Experimental investigation of graphene oxide nanofluid on heat transfer enhancement of

- pulsating heat pipe," *International Communications in Heat and Mass Transfer*, pp. 90-94, 2018 .
- [9] X. Wang, Y. He, G. Cheng, L. Shi, X. Liu and J. Zhu, "Direct vapor generation through localized solar heating via carbon-nanotube nanofluid," *Energy Conversion and Management* , pp. 176-183, 2016 .
- [10] G. Colangelo, E. Favale, P. Miglietta, A. de Risi, M. Milanese and D. Laforgia , "Experimental test of an innovative high concentration nanofluid solar collector," *Applied Energy* , pp. 874-881, 2015 .
- [11] H. Kim, J. Kim and H. Cho, "Experimental study on performance improvement of U-tube solar collector depending on nanoparticles size and concentration of Al₂O₃ nanofluid," *Energy* , pp. 1304-1312, 2017.
- [12] Y. Y. Gan, H. C. Ong, T. C. Ling, N. Zulkifli, C.-T. Wang and Y.-C. Yang, "Thermal conductivity optimization and entropy generation analysis of titanium dioxide nanofluid in evacuated tube solar collector," *Applied Thermal Engineering* , pp. 155-164, 2018.
- [13] K. Wongcharee, V. Chuwattanakul and S. Eiamsa-ard, "Influence of CuO/water nanofluid concentration and swirling flow on jet impingement cooling," *International Communications in Heat and Mass Transfer*, pp. 227-283, 2017.
- [14] M. Afrand, D. Toghraie and B. Ruhani, "Effects of temperature and nanoparticles concentration on rheological behavior Fe₃O₄-Ag/EG hybrid nanofluid: An experimental study," *Experimental Thermal and Fluid Science* , pp. 38-44, 2016 .
- [15] S. Sen , V. Govindarajan, C. J. Pelliccione, J. Wang, D. J. Miller and E. V. Timofeeva, "Surface Modification Approach to TiO₂ Nanofluids with High Particle Concentration, Low Viscosity, and Electrochemical Activity," *Applied Materials and Interfaces* , 2015 .
- [16] D. Cabalerio, C. Gracia-Fernandez, J. Legido and L. Lugo, "Specific heat of metal oxide nanofluids at high concentration for heat transfer," *International Journal of Heat and Mass Transfer*, pp. 872-879, 2015.

- [17] D. Cabalerio, L. Colla, S. Barison, L. Lugo, L. Fedele and S. Bobbo, "Heat Transfer Capability of (Ethylene Glycol + Water)-Based Nanofluids Containing Graphene Nanoplatelets: Design and Thermophysical Profile," *Nanoscale Research Letters* , 2017.
- [18] S. Bezi , B. Souayah , N. Ben-Cheikh and B. Ben-Beya, "Numerical simulation of entropy generation due to unsteady natural convection in a semi-annular enclosure filled with nanofluid," *International Journal of Heat and Mass Transfer*, pp. 841-859, 2018.
- [19] S. Pal, S. Bhattacharyya and I. Pop, "Effect of solid-to-fluid conductivity ratio on mixed convection and entropy generation of a nanofluid in a lid-driven enclosure with a thick wavy wall," *International Journal of Heat and Mass Transfer*, pp. 885-900, 2018.
- [20] M. A. Sheremet, N. C. Rosca, A. V. Rosca and I. Pop, "Mixed convection heat transfer in a square porous cavity filled with nanofluid with suction/injection effect," *Computers and Mathematics with Applications* , pp. 2665-2677, 2018.
- [21] R. Kiran Kumar and S. Varma, "MHD Boundary Layer Flow of Nanofluid Through a Porous Medium Over a Stretching Sheet with Variable Wall Thickness: Using Cattaneo–Christov Heat Flux Model," *Journal of Theoretical and Applied Mechanics*, pp. 72-98, 2018.
- [22] M. Siavashi, H. R. T. Bahrami and E. Aminian, "Optimization of heat transfer enhancement and pumping power of a heat exchanger tube using nanofluid with gradient and multi-layered porous foams," *Applied Thermal Engineering*, pp. 465-474, 2018.
- [23] A. Mwesigye, Z. Huan and J. P. Meyer, "Thermal performance and entropy generation analysis of a high concentration ratio parabolic trough solar collector with Cu-Therminol VP-1 nanofluid," *Energy Conversion and Management* , pp. 449-465, 2016.
- [24] J. Zhu, P. Chu and J. Sui, "Exact Analytical Nanofluid Flow and Heat Transfer Involving Asymmetric Wall Heat Fluxes with Nonlinear Velocity Slip," *Mathematical Problems in Engineering*, p. 12 Pages, 2018.

- [25] D. Toghraie, M. Mahmoudi, O. A. Akbari, F. Pourfattah and M. Heydari, "The effect of using water/CuO nanofluid and L-shaped porous ribs on the performance evaluation criterion of microchannels," *Journal of Thermal Analysis and Calorimetry* , pp. 145-159, 2018.
- [26] M. Siavashi, R. Yousofvand and S. Rezanejad, "Nanofluid and porous fins effect on natural convection and entropy generation of flow inside a cavity," *Advanced Powder Technology*, no. 29, pp. 142-156, 2018.
- [27] W. Guo, G. Li, Y. Zheng and C. Dong, "Numerical study of nanofluids thermal and hydraulic characteristics considering Brownian motion effect in micro fin heat sink," *Journal of Molecular Liquids* , no. 264, pp. 38-47, 2018.
- [28] A. M. Bayomy, M. Z. Saghir and T. Yousefi, "Electronic cooling using water flow in aluminum metal foam heat sink: Experimental and numerical approach," *International Journal of Thermal Science*, no. 109, pp. 182-200, 2016.
- [29] A. M. Bayomy and M. Z. Saghir, "Experimental study of using γ -Al₂O₃–water nanofluid flow through aluminum foam heat sink: Comparison with numerical approach," *International Journal of Heat and Mass Transfer*, no. 107, pp. 187-203, 2017.
- [30] A. M. Bayomy and M. Z. Saghir, "Electronic Cooling Using Finned Aluminium Heat Sink Associated with ERG Aluminium Foam: Experimental and Numerical Approach".
- [31] "Buy Al₂O₃-monodisperse spherical nanoparticles in Aqueous media | Al₂O₃-monodisperse spherical nanoparticles in Aqueous media online: MKNano.com," Mknano.com, 2019. [Online]. Available: <https://mknano.com/Nanoparticles/single-Element-Oxides/Aluminum-Oxides-Nanopowders/Al2O3-monodisperse-spherical-nanoparticles-in-Aqueous-media>.
- [32] B. Battleson, "Duocel Aluminum Foam," ERG Aerospace, 2019. [Online]. Available: <http://ergaerospace.com/materials/duocel-aluminum-foam/>.
- [33] Comsol, "COMSOL Multiphysics Modeling Software," Comsol, June 2019. [Online]. Available: <https://www.comsol.com/>.

